

Chapter 2

Iron-Based Superconductors

It is a capital mistake to theorize before one has data. Insensibly one begins to twist facts to suit theories, instead of theories to suit facts

—Sherlock Holmes, *A Scandal in Bohemia*

Two decades into the intensive study of the cuprate superconductors, the condensed-matter community got stirred up once again when another completely different family of superconductors was discovered by the group of Hideo Hosono in 2006 [1]. The Japanese group reported observation of a superconducting transition in LaFePO at a relatively low temperature of ~ 4 K. This original discovery received certain but limited attention from the community. The general excitement came 2 years later when the same group reported superconductivity at a temperature of 26 K, higher than that of most conventional superconductors, in a closely related compound LaFeAsO_{1-x}F_x at a doping level of $x = 0.12$ [2], with the parent compound LaFeAsO being non-superconducting at routinely attainable cryogenic temperatures. This latter discovery gave rise to the explosive growth of research of these materials all over the world, which led to reports of high-temperature superconductivity¹ in several new classes of compounds in this family, such as SmFeAsO_{0.9}F_{0.1} [4] ($T_c \approx 55$ K) and Ba_{0.6}K_{0.4}Fe₂As₂ [5] ($T_c \approx 38$ K).

The iron-based materials are classified based on their crystallographic structure. Separate classes are usually denoted by the chemical formula of the parent, often non-superconducting, compounds, e.g. 1111 for the parent compounds $REFeAsO$, $RE = \text{La, Sm, Gd, ...}$ or 122 for BaFe₂As₂. The most relevant and studied classes of iron-based compounds are shown in Fig. 2.1a. A common unifying feature to all these

¹ In this work we adopt the generalized definition of ‘high-temperature superconductors’ as materials with the superconducting transition temperature above 28 K (T_c of most conventional superconductors falls below this value. A well-known exception is MgB₂ with $T_c = 39$ K [3], which is a conventional, albeit a two-band superconductor). This definition differs from the historical, industrially important, notion of high-temperature superconductors as materials with T_c above the boiling point of liquid nitrogen (77 K).

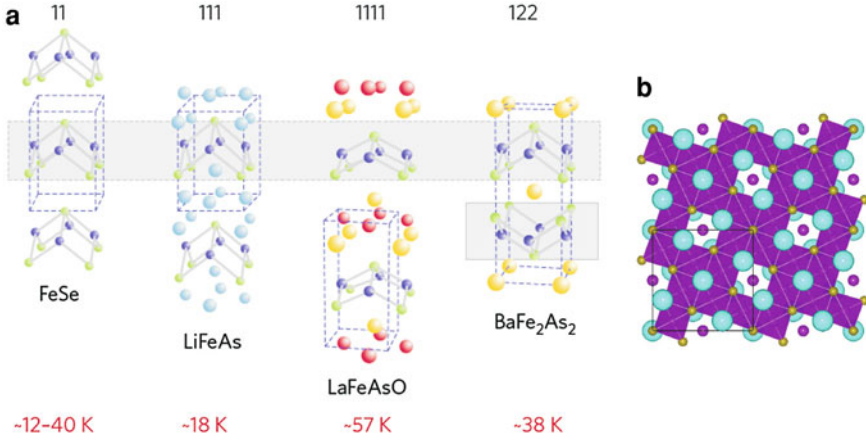


Fig. 2.1 **a** Several representative classes of the iron-based materials. The *numbers* at the *top* denote the chemical formula of the compound underneath (for instance, LiFeAs is a 111 compound), while the *temperatures* at the *bottom* specify either the superconducting transition temperature of the material itself or the highest T_c obtained by doping or substitution in a material of that type. The common structural unit of all iron-based compounds is the Fe–As tetrahedral layer (*gray areas*), with the adjacent layers either co-aligned out-of-plane or alternating in orientation. Adapted by permission from Macmillan Publishers Ltd: Nature Physics [6], copyright (2009). **b** In-plane crystallographic structure of 245 iron selenides $A_2Fe_4Se_5$ ($A = K, Rb, Cs$). Iron vacancies are depicted as *purple spheres*, selenium sites as *golden* and alkaline-metal sites as *large blue spheres*. The $\sqrt{5} \times \sqrt{5}$ enlargement of the unit cell is evident. The out-of-plane crystallographic structure is essentially identical to that of the 122 compounds. Reproduced by permission of The Royal Society of Chemistry from Ref. [7]

classes is the basic structural building block present in all iron-based materials—the Fe–As layer. This layer is composed of a square lattice of iron atoms (blue spheres in Fig. 2.1a) and an interpenetrating lattice of As atoms (green spheres) alternately displaced to above and below the plane of the iron lattice, forming almost regular tetrahedra. The difference between the classes can be reduced to the structure of the blocking layer sandwiched in between the adjacent Fe–As layers (none for the 11, monatomic for the 111 and 122, and diatomic for the 1111 compounds) and the orientation of the adjacent Fe–As layers with respect to each other (all oriented in the same direction for the 11, 111, and 1111 materials and with the alternating orientation for the 122 compounds). This work is focused on the materials in the 122 class or its generalization that encompasses the so-called vacancy-ordered 245 iron selenides $A_2Fe_4Se_5$ ($A = K, Rb, Cs$), whose general crystallographic structure is identical to that of 122 systems ($A_2Fe_4Se_5 = A_{0.8}Fe_{1.6}Se_2 \in A_{1-x}Fe_{2-y}Se_2$) but with ordered vacancies in both the intercalating-atom (x) and iron (y) sublattices (Fig. 2.1b).

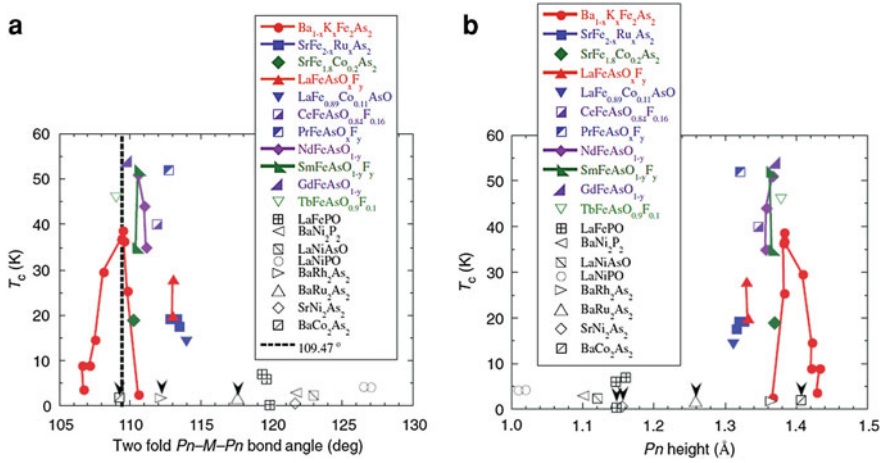


Fig. 2.2 Dependence of the superconducting transition temperature of a set of representative iron-based superconductors on the Pn–Fe–Pn bond angle (a), where Pn is a pnictogen, and on the pnictogen height (b). Adapted by permission from Taylor and Francis Ltd. (<http://www.informaworld.com>): Ref. [8], copyright (2010)

2.1 Crystallographic and Reciprocal-Space Structure

As it was shown in Fig. 1.2b, the iron-based materials exhibit three principal phases: normal (white areas), antiferromagnetic SDW (red), and superconducting (yellow). The nematic phase, shown as blue areas, is a more exotic and elusive phase, which shows no magnetism but exhibits lower point-group symmetry than the normal metallic phase. We will elaborate on the nature of this phase later on in Sect. 2.2. Since in the study reported in this thesis we have concentrated on the 122 class of the iron-based superconductors, predominantly the properties of materials pertaining to this class will be reviewed here. A more general account, as well as an extensive comparison of various structural, electronic, magnetic, and superconducting properties of several representative materials of this family can be found in excellent reviews on the topic, for instance, in Ref. [8]. A good early topical review of all current iron-based materials was given in issues 9–12 of *Physica C: Superconductivity*, 469, 313–674 (2009).

The prototypical compound of the 122 class of iron-based superconductors, and also the one that produces the highest superconducting transition temperature of 38 K upon potassium substitution, is $\text{Ba}_{1-x}\text{K}_x\text{Fe}_2\text{As}_2$ (an extensive comparison of the maximum superconducting transition temperatures and other superconducting properties of many iron-based superconductors in the 122 and other classes can be found in Ref. [9]). Other compounds in this class have been synthesized by replacing Ba with other alkali-earth metals (Sr and Ca) intercalating between the iron-arsenic layers and have properties and the phase diagram very similar to those of $\text{Ba}_{1-x}\text{K}_x\text{Fe}_2\text{As}_2$. The parent (undoped) compound of the latter is BaFe_2As_2 and

crystallizes in a ThCr_2Si_2 -type structure (see Fig. 2.1) with a tetragonal crystallographic symmetry in the $I4/mmm$ space group and two formula units per simple tetragonal unit cell [10]. The lattice parameters in the tetragonal phase at room temperature have been found to be $a = 3.9625(1) \text{ \AA}$ and $c = 13.0168(3) \text{ \AA}$ [10]. Upon cooling this compound undergoes almost coincident structural and magnetic phase transitions at $T_s \approx T_N \approx 136 \text{ K}$ into an orthorhombic (rotated around the principal tetragonal axis by 45° with respect to the tetragonal unit cell) antiferromagnetic SDW state of space group $Fmmm$ with the lattice constants $a = 5.6146(1) \text{ \AA}$, $b = 5.5742(1) \text{ \AA}$, and $c = 12.9453(1) \text{ \AA}$ [10].

This compound, like all iron-based materials due to their common iron-arsenic (or, more generally, iron-pnictogen/chalcogen) structural unit, exhibits tetrahedral coordination of Fe and As. Iron ions form a square lattice, with As ions occupying the central planar positions alternately above or below the Fe plane. The main parameter characterizing such coordination is the pnictogen height or, equivalently, the As–Fe–As bond angle. The superconducting properties of the iron-based materials have been shown to display a certain degree of correlation with these two parameters, in particular, the superconducting transition temperature tends to maximize close to the perfect tetrahedral geometry, i.e. for an As–Fe–As bond of $\arccos(-1/3) \approx 109.47^\circ$, as shown in Fig. 2.2a and, analogously for the pnictogen height, in Fig. 2.2b. Recently, first evidence for a *local* correlation between the pnictogen/chalcogen height and the rigidity of the superconducting condensate has been provided by scanning tunneling microscopy/spectroscopy (STM/STS) on FeSe thin films grown by molecular beam epitaxy [11]. Although the superconducting properties of the compounds in Fig. 2.2 obtained by aliovalent substitution are affected not only by structural distortions but also by direct chemical doping, there is significant experimental evidence that it is the structurally driven modification of the Fermi surface, rather than charge-carrier doping, which optimizes the superconducting transition temperature [12, 13].

Since some experimental probes are sensitive predominantly to Fe, rather than to all constituents, three different unit cells can often be encountered in the literature and are shown in Fig. 2.3a–c, most importantly: the 4-Fe simple tetragonal unit cell with two formula units per unit cell (Fig. 2.3a), the 1-Fe unit cell based on the Fe sublattice, which would be realized physically if all pnictogen atoms were located in the Fe plane (Fig. 2.3b), and the 2-Fe unit cell, which is the real primitive unit cell of the iron-based materials (Fig. 2.3c). These unit cells generate corresponding reciprocal unit cells, or the first Brillouin zones [14], as also shown in Fig. 2.3.

2.2 Phase Diagram

The phase diagram of all iron-based materials shows many common features and can therefore be cast into a general schematic form shown in Fig. 1.2b. The parent compounds in this family are semimetals at room temperature and exhibit an

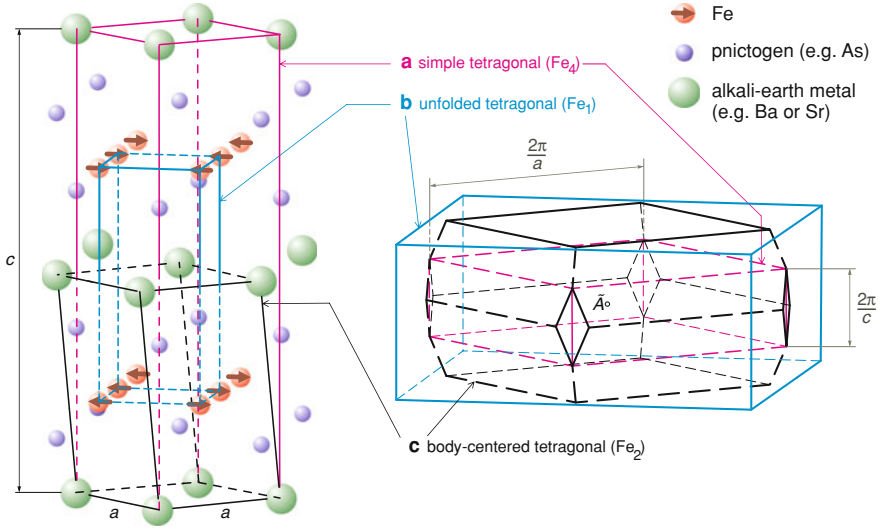


Fig. 2.3 Three different unit cells of the 122 iron pnictides: **a** the 4-Fe simple tetragonal unit cell with two formula units per unit cell, **b** the 1-Fe unit cell based on the Fe sublattice alone, and **c** the 2-Fe unit cell, which is the real primitive unit cell of the iron-based materials. Shown on the *right* are the first Brillouin zones corresponding to these unit cells. Reprinted figure with permission from Ref. [15]. Copyright (2010) by the American Physical Society. Original material obtained from and modified with permission of the author

antiferromagnetic SDW phase transition at lower temperatures.² In the rare-earth-based compounds of the 1111 class, a complex interplay of itinerant Fe and localized rare-earth moments gives rise to a sequence of (anti)ferromagnetic phase transitions [16–18], which, however, do not seem to bear significantly on the nature of superconducting pairing. What appears to be of much importance for superconductivity in these materials, and this observation correlates strongly with that in the cuprates, is the proximity to the antiferromagnetism of itinerant electrons. This proximity gives rise to strong antiferromagnetic spin fluctuations once the long-range order has been suppressed, which are currently believed to be the most plausible candidate for the superconducting pairing mediator [9, 19–25].

There are three main means of suppressing long-range antiferromagnetic order and inducing superconductivity in the iron-based compounds: aliovalent substitution [doping, e.g. $\text{Ba}_{1-x}\text{K}_x\text{Fe}_2\text{As}_2$, $\text{Ba}(\text{Fe}_{1-x}\text{Co}_x)_2\text{As}_2$; see Fig. 2.4], isovalent substitution [modification of the crystallographic structure, e.g. $\text{BaFe}_2(\text{As}_{1-x}\text{P}_x)_2$, $\text{Ba}(\text{Fe}_{1-x}\text{Ru}_x)_2\text{As}_2$], and application of external pressure. All these methods have

² with the exception of the iron-selenide compounds with vacancy ordering, which are dominated by an antiferromagnetic semiconducting phase at room temperature. Their complete classification is complicated by the fact that no single-phase superconducting compounds have been synthesized up to date and even the identification of the parent compound of this class of materials appears problematic.

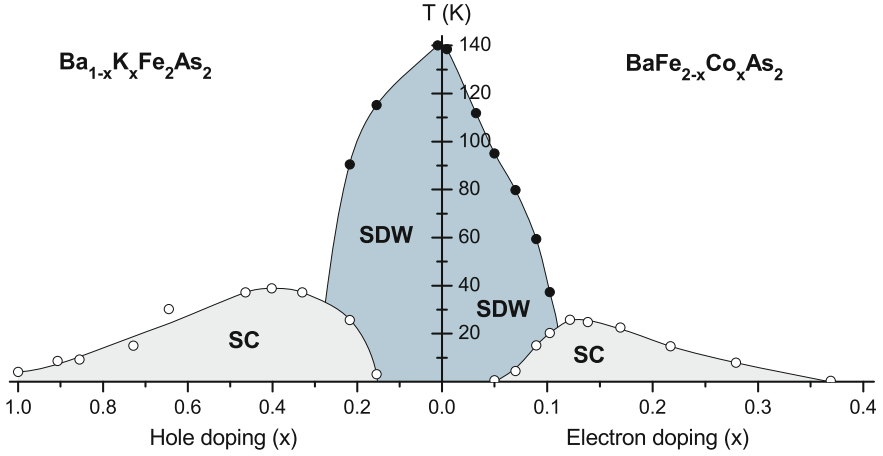


Fig. 2.4 Phase diagram of $\text{Ba}_{1-x}\text{K}_x\text{Fe}_2\text{As}_2$ (left) and $\text{Ba}(\text{Fe}_{1-x}\text{Co}_x)_2\text{As}_2$ (right). Data from Refs. [34, 35], respectively. In both series of compounds the overlap region of the SDW and superconducting phase has been found to exhibit the microscopic coexistence of the two order parameters in the single crystals of sufficiently high quality [28, 31]

been found to produce very similar results, namely, a quick suppression of long-range antiferromagnetism with subsequent induction of superconductivity in a characteristic dome-shaped region of the phase diagram [8, 26]. In certain materials a further increase of external pressure leads to a re-entrant superconducting phase with an even higher superconducting transition temperature [27].

In those iron-based compounds showing overlapping antiferromagnetic and superconducting regions of the phase diagram (see Figs. 2.2 and 2.4) the issue of phase separation/coexistence has been a topic of intense debate. At the dawn of the iron-pnictide research it was believed, for instance, that some materials, such as $\text{Ba}(\text{Fe}_{1-x}\text{Co}_x)_2\text{As}_2$, show microscopic coexistence of antiferromagnetism and superconductivity [28], whereas others, such as $\text{Ba}_{1-x}\text{K}_x\text{Fe}_2\text{As}_2$, undergo intrinsic phase separation [29]. Recently, experimental evidence in favor of microscopic phase coexistence in $\text{Ba}_{1-x}\text{K}_x\text{Fe}_2\text{As}_2$ as well as in $\text{Ba}(\text{Fe}_{1-x}\text{Ru}_x)_2\text{As}_2$ single crystals of sufficiently high quality has emerged [30–32], proving that phase separation is an extrinsic effect, at least in the 122 iron pnictides. Given that both phases coexist microscopically and homogeneously throughout the bulk of the crystal their properties must be strongly intertwined, making it possible to study the properties of one via the other. One important example in the iron-pnictide research is the type of the quantum (zero-temperature) phase transition at the boundary of the antiferromagnetic phase in the superconducting dome. If this point of the phase diagram were a quantum critical point, i.e. if the quantum phase transition from the coexistence state to the pure superconducting state were a second-order quantum phase transition, certain physical quantities would diverge. A recent study of one of the iron-pnictide compounds with phase coexistence, $\text{BaFe}_2(\text{As}_{1-x}\text{P}_x)_2$, has indeed revealed a strong

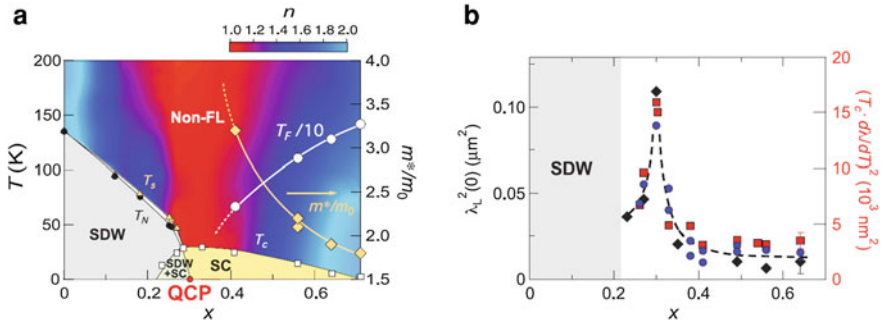


Fig. 2.5 **a** Phase diagram of $\text{BaFe}_2(\text{As}_{1-x}\text{P}_x)_2$. A quantum critical point separates the zero-temperature phase of coexisting antiferromagnetic SDW and superconductivity from the pure superconducting phase. The non-Fermi-liquid regime (red region) results from finite-temperature critical fluctuations due to the underlying quantum critical point. **b** Doping dependence of the zero-temperature London penetration depth (left vertical axis) and its temperature derivative (right vertical axis). From Ref. [33]. Reprinted with permission from AAAS

peak in the doping dependence of the zero-temperature London penetration depth $\lambda_L(0)$ at the doping level corresponding to the boundary of the coexistence phase, as shown in Fig. 2.5, thus confirming the second-order character of the corresponding phase transition [33]. The fact that the maximum of the superconducting transition temperature and the divergence of $\lambda_L(0)$ occur at the same doping level underlines the importance of critical antiferromagnetic spin fluctuations for superconductivity in the iron-based materials and reveals their dual role: critical enhancement of these spin fluctuations leads to the stronger binding of electrons into Cooper pairs and thus a higher T_c , while the concomitant increase in the scattering of electrons from these excitations makes the Cooper pairs heavier and, therefore, their screening of external magnetic fields less effective, hence the increase of the penetration depth.

Needless to say, the (thermal) phase transition from the normal to the superconducting state is of second order in the absence of an external magnetic field [36]. The transition from the normal to the antiferromagnetic state, coupled to the structural transition from the high-temperature tetragonal to the low-temperature orthorhombic phase in the 122 materials, is strongly first-order [37–41], with the exception of BaFe_2As_2 , which is believed to exhibit a weakly first-order phase transition [41]. ‘Weakly’ in this context implies that rather than being a conventional sharp discontinuous transition it extends over a sizable temperature region, giving rise to a finite resistivity anisotropy above the antiferromagnetic transition proper [41, 42].

Finally, the early discovery of resistivity anisotropy above the nominal structural transition in the parent and Co-doped BaFe_2As_2 [42, 43] has raised the question of the possible existence of another phase, at least in the 122 iron pnictides: a nematic phase, which breaks the C_4 rotational symmetry of the high-temperature tetragonal phase in a second-order phase transition. Since then, the issue of nematicity in the iron-based materials has received much attention. This new phase has been both confirmed in the Co-doped compound [44] and discovered using magnetic-torque measurements in

$\text{BaFe}_2(\text{As}_{1-x}\text{P}_x)_2$ [45]. The occurrence of the nematic phase in these compounds can be explained by anisotropic spin fluctuations above the antiferromagnetic transition temperature [46, 47]. However, the fact that in Ref. [45] the nematic phase was found to persist well into the overdoped regime of $\text{BaFe}_2(\text{As}_{1-x}\text{P}_x)_2$, far away from the long-range antiferromagnetic order, indicates that orbital anisotropy might play an important role. Recent ARPES measurements on $\text{Ba}(\text{Fe}_{1-x}\text{Co}_x)_2\text{As}_2$ provide strong support to this hypothesis [48].

2.3 Electronic Band Structure

The electronic band structure of the iron-based materials near the Fermi level is largely defined by the outer orbitals of the iron (3d) and pnictogen/chalcogen (4p) atoms. The details of the crystallographic structure and charge-carrier doping determine the exact shape of the bands and the relative location of the chemical potential and thus the geometry and topology of the Fermi surface. All iron-based compounds have been found to be multiband systems, with several separate sheets of the Fermi surface within the Brillouin zone [8, 26]. More often than not, both hole- and electron-type pockets are present, with up to a total of five. The most direct way to determine the Fermi surface of a compound is by means of ARPES. By detecting emitted electrons with the energy equal to the Fermi energy, synchrotron-based ARPES is capable of mapping the Fermi surface in the entire Brillouin zone [49]. When carried out in the superconducting state, ARPES measurements provide detailed information about the momentum-dependence of the superconducting gap on all Fermi surfaces where it can be resolved (the ultimate resolution limit is instrument-dependent, with the state-of-the-art experiments discerning superconducting gaps as small as 3 meV). When sufficiently clean single-crystalline materials are available, the Fermi surface can also be probed by various QO measurements [50].

Both ARPES and QO techniques allow for a comparison of the experimentally inferred band structure with the predictions of first-principles calculations. The information extracted from this comparison is twofold. Firstly, the overall adequacy of the *ab initio* description of a given class of materials can be assessed by comparing the gross band dispersions in the experimentally accessible energy range; the comparison of the widths of the bands tells one how strong high-energy correlations are in the system: the more compressed the experimental bands appear with respect to their calculated counterparts, the stronger the high-energy correlations are [51]. Secondly, the investigation of the deviations of the low-energy dispersion (i.e. in the vicinity of the Fermi level) from the prediction quantifies the strength of the coupling of free charge carriers to various low-energy excitations in the system, such as phonons, spin, charge and orbital fluctuations, etc. [49]. Given that the electron–electron interaction mediated by at least one type of these excitations is effectively attractive (intraband phonon-mediated interaction is always attractive), it will lead to the creation of Cooper pairs and thus the emergence of superconductivity. Since the effective mass of itinerant charge carriers in a band is defined as the second

momentum derivative of that band's dispersion at the Fermi level, any deviation of the band dispersion from the theoretical prediction implies a different effective mass, the effect called 'effective-mass renormalization'. In principle, both ARPES and QO measurements can determine this mass renormalization but in practice the latter have a much higher accuracy in this regard. In ARPES measurements, on the other hand, one can utilize different polarization states of the incident light to extract the orbital characters of the bands, which can also be compared with theoretical predictions, providing another benchmark for the adequacy of the approximations used in the calculations. More importantly, the knowledge of the orbital structure of the bands provides essential input for the more involved theories of various physical phenomena, e.g. the microscopic theory of superconductivity.

After this general discussion let us consider several concrete examples elucidating the electronic band structure of the 122 iron-based materials. The major common electronic properties of the former are well represented by the $\text{Ba}_{0.6}\text{K}_{0.4}\text{Fe}_2\text{As}_2$ compound. Figure 2.6a shows the electronic band structure of this material obtained with LDA [52] using the experimental values of the lattice constants and atomic positions in the unit cell determined by means of a Rietveld fit of powder X-ray diffraction data [10]. The different colors of the bands are used to illustrate the different orbital contributions dominating each band. It is immediately evident that

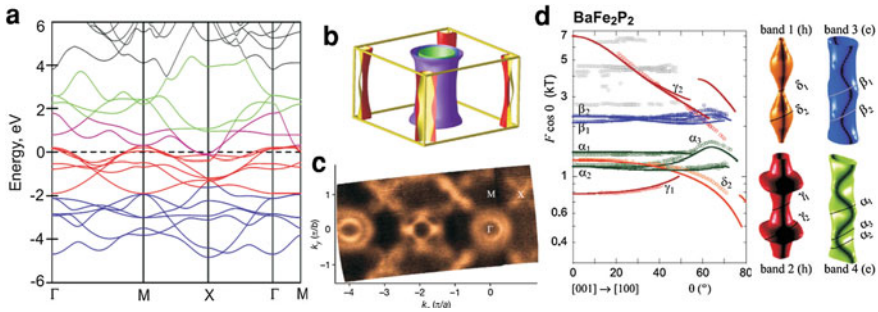


Fig. 2.6 **a** Electronic band structure of $\text{Ba}_{0.6}\text{K}_{0.4}\text{Fe}_2\text{As}_2$ obtained in LDA calculations using the experimentally determined lattice constants and atomic positions. The colors represent different dominant orbital contributions: Fe-d (red), As-p (blue), Ba-d (black); green lines denote strongly hybridized Fe-d and As-p orbitals and purple lines depict the Fe-d orbitals that give rise to the electron pockets of the Fermi surface. Adapted by permission from Macmillan Publishers Ltd: Nature Communications Ref. [52], copyright (2011). **b** Fermi surface of $\text{Ba}_{0.6}\text{K}_{0.4}\text{Fe}_2\text{As}_2$ predicted by ab initio calculations. Reprinted from Ref. [53], copyright (2009), with permission from Elsevier. **c** Its experimental counterpart obtained with ARPES. Reprinted by permission from Macmillan Publishers Ltd: Nature Ref. [54], copyright (2009). **d** Angular dependence of the QO frequencies extracted from the data obtained on a BaFe_2P_2 compound (open circles) superimposed onto the prediction of a first-principles calculation for the same compound (solid lines; the calculated bands have been shifted to match the experimental data as discussed in the text). (Far right) Partial Fermi surfaces as predicted by theory with the assignment of the QO frequencies from the left panel. Reprinted figure with permission from Ref. [55]. Copyright (2011) by the American Physical Society

the electronic structure in the vicinity of the Fermi energy (± 2 eV) is dominated by either by Fe-d (red, purple) or strongly hybridized Fe-d and As-p orbitals (green), as maintained in the introduction of this section. Deeper orbitals have mostly As-p character (blue lines), while the contribution of Ba-d orbitals becomes significant only above ~ 4 eV. The predominantly Fe-d-character bands crossing the Fermi level are holelike at the Γ point and electronlike at the X point of the 1-Fe Brillouin zone and the crossings determine the complex multiband Fermi surface of this compound shown in Fig. 2.6b. It is remarkable that, similarly to the copper–oxygen planes in the cuprates, the iron–pnictogen/chalcogen planes in the iron-based materials are only weakly coupled, making the Fermi surface two-dimensional to a large extent, with only a minor warping of its quasicylindrical sheets. Such two-dimensionality of the electronic structure is now widely believed to be one of the essential prerequisites for high-temperature superconductivity [56], mostly due to the drastic enhancement of electronic instabilities and fluctuations in lower dimensions.

The overall geometry and topology of the Fermi surface predicted by first-principles calculations as described above have been found largely consistent with experiment. All techniques sensitive to the shape of the Fermi surface have confirmed its multiband and quasi-two-dimensional character. For example, Fig. 2.6c shows the in-plane Fermi surface of $\text{Ba}_{0.7}\text{K}_{0.3}\text{Fe}_2\text{As}_2$ mapped out with ARPES. Two concentric circular pockets are clearly visible at the Γ point, along with a complex ‘propeller’ structure at the X point of the 1-Fe Brillouin zone. The latter consists of a central electronlike pocket surrounded by four ‘blades’, which have a holelike character and supposedly result from high-temperature Fermi-surface reconstruction due to a nesting instability (good match in their geometrical shape and size) between one of the circular hole pockets at the Γ point and an electron pocket at the X point of the 1-Fe magnetic Brillouin zone (M point of the 2-Fe Brillouin zone corresponding to the real chemical unit cell) [54]. Thus the topology of the ‘propeller’ structure does indeed require two electronlike pockets at the X point of the magnetic Brillouin zone, as predicted by theory (see Fig. 2.6b). Subsequent low-temperature ARPES measurements in the superconducting state of $\text{Ba}_{0.6}\text{K}_{0.4}\text{Fe}_2\text{As}_2$ have revealed three superconducting gaps centered around the Γ point, which requires three circular Fermi pockets in full agreement with *ab initio* calculations. In general, the highest-resolution reconstruction of the Fermi surface is done based on ARPES data obtained in the superconducting state. Since superconductivity gaps the entire Fermi surface symmetrically above and below (with possible nodes, i.e. points in the Brillouin zone where the superconducting gap vanishes), it is a trivial task to extract the shape of the latter from the complete momentum-dependence of the superconducting gap(s) in the Brillouin zone, which is routinely extracted from ARPES data [57, 58]. In addition, low-temperature ARPES measurements have a much higher resolution compared to those at room temperature due to the strong suppression of thermal broadening. Therefore, we postpone a more detailed review of the Fermi surface of $\text{Ba}_{0.6}\text{K}_{0.4}\text{Fe}_2\text{As}_2$ extracted from ARPES measurements until Sect. 2.5.

As outlined above, measurements of QO is a very powerful tool of condensed-matter physics and provides access to the essential properties of quasiparticle dynamics. The practical feasibility of these measurements, however, requires very clean

materials [14], which means that high doping levels are detrimental to the successful application of this technique. Unfortunately, almost all optimally doped iron-based superconducting materials showing the highest superconducting transition temperature are relatively heavily doped/substituted. In addition, QO can only be observed in a metallic compound with a finite Fermi surface. Therefore, superconductivity must be fully suppressed by applying a magnetic field above the upper critical field to recover the normal state and allow for QO measurements. This fact makes such experiments very challenging to perform on optimally doped iron-based superconductors because many of them show upper critical fields above 150 T [8]. Such magnetic fields are inaccessible even to the most powerful state-of-the-art pulsed magnets. The above limitations clarify why the overwhelming majority of QO measurements have been carried out on the end members of various doping series. Since all undoped iron-based compounds are itinerant antiferromagnets, their low-temperature Fermi surface is dramatically reconstructed with respect to the normal state, making the utility of the extracted data quite limited (for a review of the QO measurements on 122 parent compounds see, e.g., Ref. [50]). It thus comes as no surprise that the most insightful experiments up to date have been carried out on the extremely overdoped and the end members of the $\text{BaFe}_2(\text{As}_{1-x}\text{P}_x)_2$ series. An exemplary set of experimental data obtained on BaFe_2P_2 and a comparison to the corresponding ab initio calculations carried out for the same compound [55] are shown in Fig. 2.6d. The observation of multiple frequency sets in the Fourier-transformed raw data clearly confirms the multiband character of this iron pnictide. The schematic partial Fermi surfaces on the right demonstrate how these frequencies and their angular dependence can be assigned to different hole and electron Fermi pockets of the theoretically predicted band structure. The solid lines in the figure correspond to the angular dependence of the QO signal predicted by the DFT calculation, displaced by +68/+58 meV for the inner/outer electron sheets and -113 meV for the inner hole sheet [55]. The band displacements required to reconcile the first-principles results with the experimental data on BaFe_2P_2 are quite close to those inferred from the analogous analysis of the data obtained on SrFe_2P_2 compounds [59, 60]. It is clear from the comparison in Fig. 2.6d that apart from the band shifts the agreement of experiment and theory is remarkable, implying that the calculation captures the out-of-plane shape of the Fermi surface rather well. Very similar results and conclusions have been obtained for intermediate phosphorus doping levels within the same series [61, 62]. Finally, the renormalization of the quasiparticle mass m^*/m_{band} can be determined from the comparison of the effective quasiparticle mass m^* extracted from the temperature dependence of the QO signal at a particular angle with the effective mass m_{band} predicted by DFT calculations. At terminal phosphorus doping levels this renormalization is of order 2 and largely uniform for all orbitals [60] but gets enhanced to ~ 4 for certain orbitals upon approaching the superconducting phase [62].

2.4 Magnetic Properties

The proximity of superconductivity to strong antiferromagnetism, observed in both the cuprate and the iron-based superconductors, is believed to be another key prerequisite for high-temperature superconductivity [56], along with the two-dimensionality of the Fermi surface discussed above. Although the antiferromagnetic phases are quite different in the cuprates and pnictides, one thing is common: the antiferromagnetic and superconducting order parameters appear to compete in their fully ordered forms but superconductivity is strongest where the antiferromagnetic long-range order has just disappeared completely. This suggests that, although superconductivity is destroyed by long-range antiferromagnetic order, it is in fact driven by the fluctuations of electron spins, which are strongest (but already weak enough not to give rise to the competing long-range order) at the border with the antiferromagnetic phase. A large body of experimental data strongly supports this conclusion: INS revealed a resonance mode, similar to the one observed in the cuprate superconductors, at the value of the antiferromagnetic ordering vector in all iron-based superconductors [8]; the signatures of the mediating boson, glueing Cooper pairs together, revealed with other techniques are also largely consistent with the energy of this resonance mode [21, 23, 63]. This makes the study of the magnetic properties of the iron-based materials indispensable to a complete understanding of their superconducting pairing mechanism.

2.4.1 Antiferromagnetic Ground State

The ground state of the antiferromagnetic phase has been studied in detail in all known iron-based compounds by means of neutron scattering techniques. The literature on the subject is extensive and has already been reviewed, for instance, in Ref. [8]. Therefore, it appears more instructive to review the most relevant to the subsequent discussion characteristic common features of antiferromagnetism in the iron-based materials through the prism of the dichotomy between its local and itinerant character, which so far has received less attention (this discussion is to some extent based on Ref. [64]). To compare these two manifestations of magnetism and to what extent they relate the cuprate and iron-based materials, one first needs to define them. Magnetism is called *local* if the magnetic state results from the ordering of the already present in the normal state local magnetic moments of the electrons from the outer shell of one of the atomic species comprising the crystal lattice. These moments are usually large because each unpaired electron spin contributes $0.5 \mu_B$ to the total moment. This type of magnetism is most clear in insulating compounds since the absence of delocalized (itinerant) electrons makes all magnetic moments localized. The parent compounds of the cuprate superconductors, being inherent Mott insulators (i.e. their insulating behavior is due to very strong electron–electron correlations [51]; most of these compounds emerge as metals in

first-principles calculations, which do not fully account for correlations), constitute a good example of local antiferromagnets. Figure 2.7a shows the diagonal-stripe antiferromagnetic ground state of one of the cuprate parent compounds: La_2CuO_4 . It has a sizable magnetic moment of $0.5 \mu_B$ [68], consistent with its local character. The magnetic Bragg peaks formed by this periodic arrangement of the local magnetic moments are located at the $(\pm\pi, \pm\pi)$ points of the first Brillouin zone, shown in Fig. 2.7e (or $(1/2, 1/2)$ reciprocal lattice units in the $[\text{H}, \text{K}]$ notation of the two-dimensional reciprocal space $(2\pi/a, 2\pi/b, 2\pi/c)$ used in the figure). Since the cuprate parent compounds are insulating, whereas superconductivity clearly requires itinerant electrons to exist for them to eventually get bound into delocalized Cooper pairs, doping of either type (electron or hole) is necessary to induce superconductivity in these materials. As a matter of example, and to demonstrate the single-band character of superconductivity in the cuprates, we show the Fermi surface of a slightly doped ($x = 0.07$) but not yet superconducting $\text{La}_{1-x}\text{Sr}_x\text{CuO}_4$. This material shows a single large electronlike Fermi pocket centered at the corners of the Brillouin zone.

In contrast, magnetism is called *itinerant* if the magnetic state results from spontaneous self-organization of the itinerant-electron spin density into a periodic magnetic structure, called a spin-density wave. In this type of magnetism, no magnetic moment needs to be present in the normal state (and it is often not), since the ionic shells and the itinerant-electron spin density can both be spin-compensated. Moreover, the value of the ordered magnetic moment can be much smaller than in the local case because (a) not all itinerant electrons might participate in the formation of this moment and (b) the total number of free electrons can be much smaller in the case of a doped (rather than inherently metallic) material. The aforementioned spontaneous formation of a finite itinerant magnetic moment results from a nesting instability (good geometrical match in the shape) between two sheets of the Fermi surface [69], which is generally strongly enhanced by the low dimensionality of the latter. A classical example of a purely itinerant antiferromagnet is elemental chromium [70].

The situation in the iron-based compounds is significantly more complex. It is currently believed that these compounds are located between purely local magnets like the cuprates and purely itinerant magnets like elemental chromium [64].

Indications of the itinerant character of antiferromagnetism in the iron-pnictides:

- Moderate electronic correlations. The degree of electron–electron correlations can be assessed by directly comparing the band structure obtained in LDA calculations (which neglects most of electronic correlations) with experiment, such as ARPES or QO measurements, as well as by comparing the kinetic energy of itinerant charge carriers approximated by the partial f -sum rule for the optical conductivity [71] in experiment and theory. In both cases one arrives at the same conclusion that the electronic correlations in iron-based materials are moderate and therefore unlikely to create distinct local moments like in the cuprate materials.
- Nesting is good in most compounds. It has been predicted by first-principles calculations and largely confirmed by extensive ARPES measurements that most of iron-based compounds exhibit rather good nesting between hole- and electron-like pockets of the Fermi surface, making them prone to a spin-density-wave

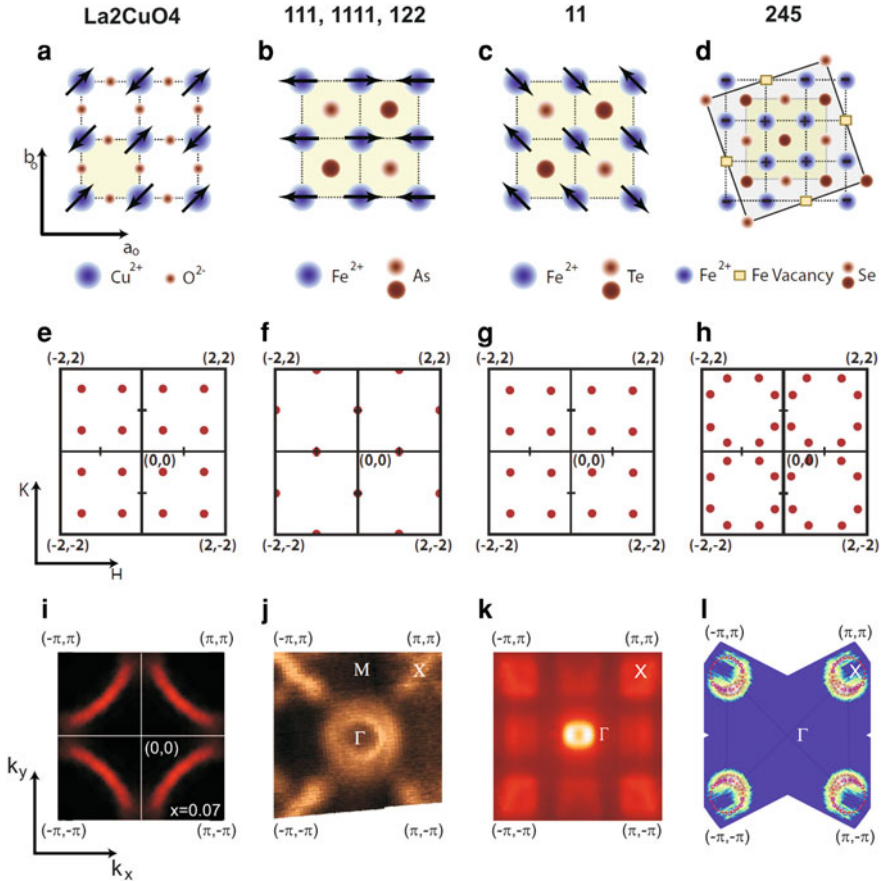


Fig. 2.7 **a–d** Antiferromagnetic ground state of several representative parent compounds of the cuprate and iron-based superconductors: La_2CuO_4 (**a**); LiFeAs (111), LaFeAsO (1111), and BaFe_2As_2 (122)—panel (**b**); FeTe (11)—panel (**c**); $\text{K}_2\text{Fe}_4\text{Se}_5$ (245)—panel (**d**). The chemical unit cell (in the case of La_2CuO_4) and the pseudotetragonal unit cell (which approximates the low-temperature orthorhombic unit cell, with the lattice parameters $a_{\text{ort}} \approx b_{\text{ort}} \approx \sqrt{2}a_{\text{tet}}$) are shown in *light green*. **e–h** Magnetic Bragg peaks in the reciprocal space of the respective unit cells marked in *green*. **i–l** Corresponding Fermi surfaces in the normal state (above the magnetic transition temperature) obtained with ARPES: **i** $\text{La}_{2-x}\text{Sr}_x\text{CuO}_4$ at a doping level of $x = 0.07$; **j** $\text{Ba}_{1-x}\text{K}_x\text{Fe}_2\text{As}_2$ at a doping level of $x = 0.3$; **k** FeTe ; **l** $\text{K}_2\text{Fe}_4\text{Se}_5$. In all cases, the Brillouin zone depicted corresponds to the chemical unit cell of the compounds (comprising two Fe atoms (Fig. 2.3c) in the case of iron-based materials), whereas the characteristic points in the reciprocal space (Γ , X , and M) belong to the unfolded Brillouin zone, which corresponds to the unit cell of the iron sublattice comprising one Fe atom (Fig. 2.3b; relevant to magnetic scattering experiments). Panels **a–h** reprinted by permission from Macmillan Publishers Ltd: Nature Physics Ref. [64], copyright (2012). Panels **i**, **k**, and **l** are figures reprinted with permission from Refs. [65–67], respectively. Copyright (2006, 2009, 2011) by the American Physical Society. Panel **j** reprinted by permission from Macmillan Publishers Ltd: Nature Ref. [54], copyright (2009). In panels **i**, **k**, and **l**, the original Fermi surface maps have been symmetrized according to the (pseudo)tetragonal symmetry to cover the entire first Brillouin zone

instability. Figures 2.7j, k show well-nested quasicircular hole and electron sheets of the Fermi surface in four major classes of iron-based materials. In the case of $\text{Ba}_{1-x}\text{K}_x\text{Fe}_2\text{As}_2$ the high-temperature Fermi-surface reconstruction has already distorted the otherwise circular shape of the outer electron Fermi pocket into ‘blades’ (Fig. 2.7j and the discussion above).

- Observed ordered antiferromagnetic moment is small in most compounds. In 111, 1111, and 122 compounds the ordered antiferromagnetic moment of $0.3\text{--}1.0\mu_{\text{B}}$ [8] is quite small, bearing in mind that there are six electrons in the Fe-3d orbital.
- Spin-wave dispersion is significantly broadened at high energies [72]. The broadening can be ascribed to particle-hole excitations across the Fermi surface, as supported by RPA calculations in an itinerant model [73]. In a stark contrast to this broadening is the instrumental-resolution-limited spin-wave dispersion of La_2CuO_4 [74].

Indications of the local character of antiferromagnetism in the iron-pnictides:

- Observation of different antiferromagnetic ground states in the iron-based compounds although their Fermi surfaces are generally very similar: Figures 2.7j, k show that for 111, 1111, 122, and 11 materials the Fermi surface shows the best nesting along the $\Gamma\text{--}X$ direction in the unfolded magnetic 1-Fe Brillouin zone, which implies the $(\pi, 0)$ ordering vector and the presence of the corresponding Bragg peak in the reciprocal space. Whereas in the 111, 1111, and 122 materials this is indeed the case, as shown in Fig. 2.7f, for 11 compounds the Bragg peaks are located at $(\pm\pi/2, \pm\pi/2)$ points of the magnetic Brillouin zone, in a stark disagreement with the nesting picture.
- Observation of a sizable Fe magnetic moment even at room temperature for most iron-based materials, which is, moreover, comparable to its ordered counterpart. Such observations have been made even for compounds that do not order magnetically at any temperature (e.g. LiFeAs) [64, 75].
- ARPES on LiFeAs shows no nesting but, nevertheless, a sizable bandwidth renormalization of ~ 3 [64, 76]. On the other hand, LiFePO shows a rather good nesting but no magnetic order [64].

All these considerations strongly indicate that antiferromagnetism in iron-based compounds has a strongly dual character with the signatures of both local and itinerant magnetic moments.

2.4.2 Spin Fluctuations

In superconducting compounds, even in those where superconductivity coexists with antiferromagnetism, all itinerant electrons that do not participate in itinerant magnetism but rather get bound into superconducting Cooper pairs are in a paramagnetic state. Although the ordered magnetic moment is zero in an itinerant paramagnet, statistical fluctuations of electron-spin density may still be significant [77]. Depending on the time scale of these fluctuations in a given material they can be detected

by various techniques such as INS, NMR, μ SR, etc. In the iron-based superconductors, just like in their cuprate counterparts, such spin fluctuations have indeed been observed and have been shown to occur at the same wave vector in the Brillouin zone as the static magnetism of the respective parent compounds [9, 20]. The properties of spin fluctuations in the 122 iron arsenides in the normal and superconducting state have been extensively discussed in Ref. [15]. The authors have shown that the symmetry and the in-plane anisotropy of these spin fluctuations are well captured by density-functional and itinerant-electron calculations in the random-phase approximation and can be traced back to the structural properties of the host compounds without invoking exotic nematic scenarios with a symmetry-broken electronic state.

2.5 Superconducting Properties

While the mechanism of superconductivity in the iron-based superconductors is under debate, it has been shown theoretically that the electron–phonon coupling in these compounds is very weak and thus unable to account for the observed high superconducting transition temperatures [78] (for an overview of the superconducting gaps and transition temperatures of a large set of iron-based superconductors see Ref. [9]). On the other hand, theoretical treatment has shown that spin fluctuations can, in principle, lead to an *effective* attractive interaction between itinerant electrons and thus to their pairing and the formation of a superconducting condensate [79]. A large body of experimental data obtained on compounds from both the cuprate and the iron-pnictide family of superconductors strongly supports this mechanism of superconductivity [21, 23, 63, 80], making spin fluctuations the most plausible candidate for the so-called ‘superconducting pairing glue’ or ‘mediating boson’. In Sect. 4.2 we will provide evidence supporting this statement based on the analysis of the optical conductivity of $\text{Ba}_{0.68}\text{K}_{0.32}\text{Fe}_2\text{As}_2$ in the framework of the Eliashberg theory, the most complete theory of superconductivity to date.

Since the bare electron–electron interaction mediated by spin fluctuations is repulsive [82], no formation of Cooper pairs can occur in the simplest *s*-wave pairing channel (i.e. with a sign-constant superconducting gap). This is true for any pairing–mediating interaction based on the general form of the gap equation. In the simplest case of the BCS theory of superconductivity the latter reads:

$$\Delta_{\mathbf{k}} = -\frac{1}{2} \sum_{\mathbf{l}} V_{\mathbf{kl}} \frac{\Delta_{\mathbf{l}}}{\sqrt{\xi_{\mathbf{l}}^2 + \Delta_{\mathbf{l}}^2}},$$

where $\Delta_{\mathbf{k}}$ is the momentum-dependent superconducting energy gap, $V_{\mathbf{kl}}$ is the reciprocal-space matrix element of the interaction potential, and $\xi_{\mathbf{k}}$ is the one-electron energy at momentum \mathbf{k} relative to the chemical potential. Given that the potential V of a repulsive interaction is positive, in the case of spin-fluctuation-mediated pairing this relation can obviously only be fulfilled if the gap changes sign in some part

of the Brillouin zone. This conclusion is further supported by the observation of a resonance enhancement of the spin-fluctuation spectrum below 2Δ in the superconducting state [9, 19, 20, 22, 83–86] (see also Fig. 2.10). According to the algebraic structure of the magnetic scattering intensity with respect to the coherence factors of the superconducting condensate [36], such a resonance can only occur if $\Delta_{\mathbf{k}}$ changes its sign across the Brillouin zone (although recently it has been demonstrated that a similar peak structure in INS spectra can arise, albeit at a somewhat different characteristic energy, even in the case of a sign-constant superconducting gap [87]). For the multiple-sheet Fermi surface of the iron-based superconductors this implies that the sheets coupled by the repulsive spin-fluctuation-mediated interaction must host superconducting gaps of different sign. If, in addition, the gap on each Fermi surface complies with the tetragonal symmetry of the compound and is sign-constant on the sheets at the center of the Brillouin zone, such a pairing symmetry is called extended s -wave symmetry or s_{\pm} symmetry, where \pm implies that the gap changes its sign from sheet to sheet. In general, tetragonal symmetry D_{4h} allows for four different symmetries of the superconducting order parameter on a single-sheet Fermi surface in the singlet pairing channel [88]. A schematic representation of these superconducting order parameters in the Brillouin zone, together with the group-theoretical notation, wave function notation, and the corresponding basis functions is given in Fig. 2.8. The situation becomes more complex in a multiband case, giving rise to various ‘extended’ symmetries of the aforementioned four basic types.

While the determination of the relative sign of the superconducting gap across the Fermi surface is a very difficult task and requires sophisticated phase-sensitive experiments [89–91], its magnitude is readily accessible to a broad variety of experimental techniques, such as ARPES, scanning tunneling spectroscopy (STS), Andreev reflection spectroscopy, optical spectroscopy, and many others. In this regard it is

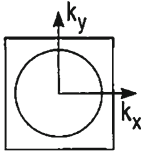

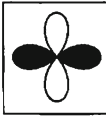
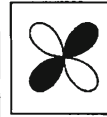
Group-theoretic notation	A_{1g}	A_{2g}	B_{1g}	B_{2g}
Order parameter basis function	constant	$xy(x^2-y^2)$	x^2-y^2	xy
Wave function name	s -wave	g	$d_{x^2-y^2}$	d_{xy}
Schematic representation of $\Delta(\mathbf{k})$ in B.Z.				

Fig. 2.8 Four symmetries of the superconducting order parameter in the singlet pairing channel allowed by the tetragonal D_{4h} crystallographic symmetry. *Different colors* in the schematic representation of the momentum dependence of the superconducting gap in the Brillouin zone indicate its different signs. Reprinted figure with permission from Ref. [81]. Copyright (2000) by the American Physical Society

important to remember that each technique measures its own *effective* superconducting gap averaged over a certain portion of the Fermi surface, which requires careful extraction of the inherent microscopic gap (when it is possible at all) through modeling of experimental spectra. Since any complex modeling increases the uncertainty of the magnitude of the extracted quantity, it is highly desirable to be able to obtain the value of the superconducting gap with as little data processing as possible. ARPES has the unique capability of not only extracting the value of the superconducting gap with minimal data analysis but also mapping it out for the Fermi surface in the entire Brillouin zone. The knowledge of the complete momentum-dependent superconducting energy gap $\Delta_{\mathbf{k}}$ is indispensable to an adequate theoretical description of superconductivity. As of today, ARPES measurements have already been carried out on most iron-based superconductors [8] and the values of their superconducting gaps have been determined (see Ref. [9] for a digest of the superconducting gaps of the iron-based superconductors obtained with various experimental techniques). In the case of $\text{Ba}_{0.6}\text{K}_{0.4}\text{Fe}_2\text{As}_2$, the most complete momentum dependence of the superconducting gap has been given in Refs. [57, 58] and is reproduced in Fig. 2.9. Several characteristic features of the superconducting gap common to all iron-based materials are immediately apparent: first, since superconductivity gaps the Fermi surface in its

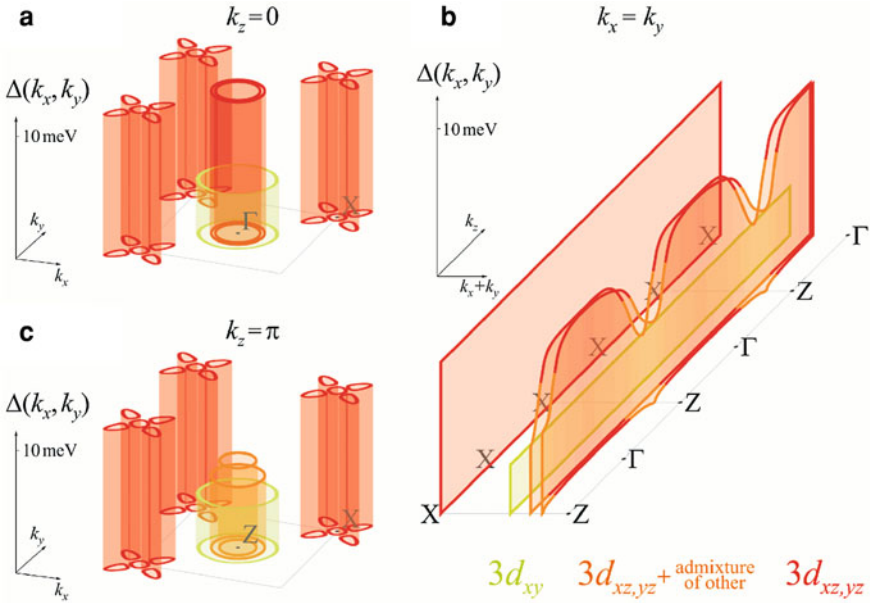


Fig. 2.9 **a** Schematic representation of the momentum-dependent superconducting energy gap of $\text{Ba}_{0.6}\text{K}_{0.4}\text{Fe}_2\text{As}_2$ obtained with ARPES at $k_z = 0$. **b** Same for $k_z = \pi$. **c** Momentum dependence of all superconducting gaps in the out-of-plane direction across several Brillouin zones. Colors indicate the magnitude of the superconducting gap (increasing from green to red). Characteristic points in the Brillouin zone refer to the one-iron unit cell of the Fe sublattice. Adapted with author's permission from Ref. [58]

entirety, the existence of multiple electronic bands implies multiple superconducting gaps, and they have indeed been observed; second, the overwhelming majority of the iron-based superconductors exhibit a certain clustering of the magnitudes of the superconducting gaps into two groups. Fig. 2.9a shows how the superconducting gap on the inner two holelike Fermi surfaces at the Γ point and on both Fermi surfaces at the X point of the unfolded 1-Fe Brillouin zone have approximately the same value of 10 meV, whereas on the outer holelike Fermi surface at the Γ point it is significantly smaller, ≈ 3.5 meV. Although most of the iron-based superconductors, including $\text{Ba}_{1-x}\text{K}_x\text{Fe}_2\text{As}_2$, exhibit a largely two-dimensional Fermi surface, the dependence of one of the large superconducting gaps on the out-of-plane momentum \mathbf{k}_z shows significant variation, with the magnitude of the gap decreasing by a factor of 3 at $\mathbf{k}_z = \pi$ to match the small gap (see Figs. 2.9b, c). This unexpected out-of-plane dependence of the superconducting gap is at odds with the two-dimensional, cylindrical in the out-of-plane direction, Fermi surface of $\text{Ba}_{0.6}\text{K}_{0.4}\text{Fe}_2\text{As}_2$ and strongly suggests that the orbital character of the bands making up the Fermi surface plays a very important role in the mechanism of superconductivity of the iron-based materials. This conclusion is further supported by recent observations of orbital-dependent electronic properties of these compounds [24, 47, 48, 92–94] and several theoretical proposals for an orbital-fluctuation pairing mechanism have been put forward [95, 96].

Although the value of Δ does characterize the energy gap in the quasiparticle excitation spectrum of a superconductor [36], it does not provide direct evidence for the *strength* of the pairing, or how tightly electrons are bound together into Cooper pairs.³ Determination of the pairing strength is difficult and in most cases involves a significant amount of modeling, although in some cases some insight can be gained already from a simple comparing of the raw data. For instance, by comparing the fingerprints of superconductivity in specific-heat data obtained on high-quality $\text{Ba}_{0.68}\text{K}_{0.32}\text{Fe}_2\text{As}_2$ single crystals to those of well-known superconductors, P. Popovich et al. came to the conclusion that this particular compound is a strongly-coupled superconductor [21]. Similar analysis has been applied to $\text{Ba}(\text{Fe}_{1-x}\text{Co}_x)_2\text{As}_2$ [97] and other iron-based compounds. The strength of the superconducting pairing interaction can also be determined from the quasiparticle effective-mass renormalization, which can be inferred from QO measurements, as discussed earlier in this chapter. In general, the cyclotron effective-mass renormalization (relevant to the QO technique) of free charge carriers can be defined as $m^*/m_{\text{band}} = 1 + \sum_i \lambda_i$, where λ_i is the coupling constant characterizing the interaction strength of electrons with all other bosonic excitations existing in the system (phonons, spin or orbital fluctuations, excitons, etc.) [98, 99]. One should be very cautious, however, because all interactions, including those that do not lead to superconducting pairing or might even weaken it, contribute to this effective-mass renormalization. Therefore, QO measurements only provide the upper bound on the superconducting pairing strength.

³ Although the superconducting gap does depend on the coupling strength, its dependence on other quantities complicates the extraction of the pairing strength alone [36].

One of the simplest but at the same time the roughest ways to gauge the superconducting coupling strength directly is by computing the ratio $2\Delta/k_B T_c$. While in the single-band case of the BCS theory this gap ratio does not depend on λ and is equal to 3.5, in the multiband case it does acquire a certain dependence on λ [100]. However, already in the two-band case with purely interband interaction the BCS theory gives qualitatively incorrect results at all coupling strengths (even in the weak-coupling limit) due to the complete neglect of the quasiparticle mass renormalization via the pairing interaction. The multiband BCS theory must, therefore, be dismissed in favor of the more complete Eliashberg theory of superconductivity. The latter predicts that the gap ratio grows monotonously with the coupling strength even in the multiband case [101]. This monotonous dependence allows one to estimate the coupling strength by taking a ratio of two easily accessible in experiment quantities: the superconducting energy gap and transition temperature. A comparison of gap ratios for a large number of various superconducting compounds has been carried out in Ref. [9] and revealed that iron pnictides are located between the cuprate and the conventional superconductors with respect to the coupling strength but show significant variation, spanning the range from weak to intermediate coupling.

Both spin fluctuations and Cooper pairs are hosted by the same electronic subsystem, namely, itinerant electrons. Therefore, it comes as no surprise that the development of the superconducting state should have a strong effect on the properties of spin fluctuations, irrespective of the source of the pairing interaction. Such a feedback effect has been observed experimentally in many different families of superconductors and consists in the opening of a spin gap in the spin-fluctuation spectrum, as illustrated in Fig. 2.10 for the case of $\text{BaFe}_{1.85}\text{Co}_{0.15}\text{As}_2$ and $\text{Ba}_{0.6}\text{K}_{0.4}\text{Fe}_2\text{As}_2$. Upon entering the superconducting state the low-energy spectrum of spin fluctua-

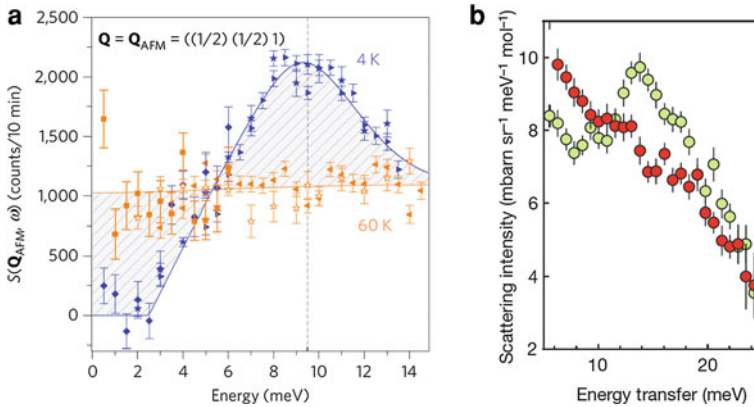


Fig. 2.10 **a** Magnetic scattering function of $\text{BaFe}_{1.85}\text{Co}_{0.15}\text{As}_2$ in the normal and superconducting state at 60 and 4 K, respectively, after a background correction. Reprinted by permission from Macmillan Publishers Ltd: Nature Physics Ref. [20], copyright (2009). **b** Neutron scattering intensity (cross-section) from $\text{Ba}_{0.6}\text{K}_{0.4}\text{Fe}_2\text{As}_2$ in the normal and superconducting state at 50 and 7 K, respectively. Reprinted by permission from Macmillan Publishers Ltd: Nature Ref. [19], copyright (2008)

tions shows dramatic enhancement below 2Δ at a characteristic frequency ω_{res} , with a concomitant suppression at even lower frequencies. Due to the conservation of the total electron spin in the system, the total spectral weight (the area under the curve) of the magnetic scattering function $S(\mathbf{Q}, \omega)$ ⁴ does not change between the normal and the superconducting state. A peak in the spin-fluctuation spectrum only occurs if the coherence factors of the magnetic dipole interaction interfere constructively, which requires that the superconducting gap change its sign across the Fermi surface, as mentioned above. The above discussion holds true for any type of pairing interaction. If, however, superconducting pairing is mediated by spin fluctuations themselves, a successful theory of superconductivity would have to account for this feedback effect self-consistently. Unfortunately, it introduces a significant degree of additional complexity into the problem and makes its handling challenging. If only a qualitative description of superconducting properties is sought, then, to the first approximation, the feedback effect of superconductivity on spin fluctuations can be neglected, as it will be done in the analysis of the far-infrared conductivity of $\text{Ba}_{0.68}\text{K}_{0.32}\text{Fe}_2\text{As}_2$ in the superconducting state in Sect. 4.2. Some of the consequences of the feedback effect for the optical conductivity of superconductors have been addressed in Ref. [102].

2.6 Properties of the $\text{A}_2\text{Fe}_4\text{Se}_5$ -Type Compounds ($\text{A} = \text{K}, \text{Rb}, \text{Cs}$)

After the discovery of the 122 iron pnictides [5], massive research effort has been made to identify and characterize other compounds of this family. Numerous elements of the periodic table have been used for doping or substitution and as the base elements of parent compounds [8]. In the former case, both aliovalent substitution resulting in doping with holes [$\text{Ba}_{1-x}\text{K}_x\text{Fe}_2\text{As}_2$, $\text{Ba}_{1-x}\text{Na}_x\text{Fe}_2\text{As}_2$] and electrons [$\text{Ba}(\text{Fe}_{1-x}\text{Co}_x)_2\text{As}_2$, $\text{Ba}(\text{Fe}_{1-x}\text{Ni}_x)_2\text{As}_2$] and isovalent substitution changing the electronic structure without affecting the position of the Fermi level [$\text{Ba}(\text{Fe}_{1-x}\text{Ru}_x)_2\text{As}_2$, $\text{BaFe}_2(\text{As}_{1-x}\text{P}_x)_2$] have been explored. In the search of new parent compounds several chemical elements have been considered as intercalants: Ca, Sr, and Ba have all produced compounds with quite similar gross physical properties although certain subtle changes have been discovered upon more detailed scrutiny [8]. In all cases the synthesis of single-phase materials throughout the entire phase diagram has been achieved, with superconductivity and antiferromagnetism coexisting on a microscopic level in its certain regions [28]. Until late 2010 only Fe–As-based compounds had existed in the 122 class of the iron-based materials, when at the very end of the year a new type of the 122 compounds based on Fe–Se

⁴ The magnetic scattering function is connected to the differential neutron scattering cross-section (intensity) per atom via $d^2\sigma/Nd\Omega dE_f = (k_f/k_i) |b|^2 S(\mathbf{Q}, \omega)$, where N is the total number of atoms, Ω is the scattering solid angle, E_f is the final energy, $k_{f,i}$ is the final (initial) wave vector of neutrons, and b is the scattering length.

layers was discovered and reported to have a superconducting transition temperature as high as 32 K [103–108]. Three members of this $A_x\text{Fe}_{2-y}\text{Se}_2$ class, differing only in the intercalating atom ($A = \text{K}, \text{Rb}, \text{and Cs}$), have been successfully synthesized and extensively studied. These compounds were conceived as an extension of the 122 class of the iron arsenides and were expected to share most of the common characteristics of the latter. However, very soon it has been realized that, although the crystallographic structure of the 122 iron arsenides and chalcogenides was in many respects alike, many physical and chemical properties have been found to differ drastically. Even though the new superconductors displayed a rather high superconducting transition temperature, comparable to the optimally 122 iron arsenides, in the former this transition temperature was achieved *without* any doping or substitution and turned out to be independent of the intercalating alkaline metal [103–105, 108]. The microstructural properties of the Fe–Se layer were also found to remain largely unaffected by the choice of the intercalating atom [109]. Further, unlike the single-phase 122 iron arsenides, these new compounds have defied all efforts to synthesize a bulk single-phase material. Granted that this could be taken as the indication of the relatively low quality of single crystals synthesized to date, there is significant experimental evidence that phase separation in the 122 iron chalcogenides is essentially inherent in its nature, as will be discussed at the end of this section and in Sect. 4.4.

Subsequent extensive bulk-sensitive measurements of the 122 iron chalcogenides revealed that, although the superconducting *shielding* volume fraction inferred from ac susceptibility measurements in the best-quality compounds approached 100 % [22, 110] (100 % diamagnetic shielding implies $4\pi\chi = 1$ in the zero-field-cool configuration), its actual fraction made up only 10–20 % of the sample volume [111–114], immediately implying that superconductivity in these materials bears a percolating character. This conclusion was later confirmed in a study of the dependence of the morphology of the superconducting-phase network in potassium-doped compounds on crystal growth parameters and post-processing [115]. The existence of phase separation in the 122 iron chalcogenides has now been observed by practically every experimental technique [27, 111–114, 116–130] and is thus reliably established. Quite interestingly, phase separation in the out-of-plane direction was discovered to occur on the nanoscale in the shape of quasiregularly alternating layers of the superconducting and antiferromagnetic phase [114].

Given that the superconducting phase occupies a very small fraction of the sample volume, some of its properties remained elusive for almost 2 years of intensive research. Therefore, we first review the main features of the antiferromagnetic majority phase, which have all been established robustly soon after the discovery of these compounds. Already the first structural refinement of single-crystal X-ray diffraction data obtained on these compounds has revealed that, unlike the tetragonal $I4/mmm$ symmetry of ThCr_2Si_2 type found in all 122 iron arsenides at room temperature, an inherent iron-deficiency order with a chiral $\sqrt{5} \times \sqrt{5} \times 1$ superstructure, present in these materials, reduces the symmetry to $I4/m$ and makes it more appropriate to classify them into the 245 stoichiometry [7] (e.g. $\text{Rb}_2\text{Fe}_4\text{Se}_5$), with the lattice parameters being $a = 8.7653(2) \text{ \AA}$, $c = 13.8811(5) \text{ \AA}$. The in-plane structure, including iron vacancies and the $\sqrt{5} \times \sqrt{5}$ -reconstructed unit cell (black rectangle),

is shown in Fig. 2.1b. The out-of-plane crystallographic structure is identical to the 122 iron arsenides (see Fig. 2.1a). Such a $\sqrt{5} \times \sqrt{5} \times 1$ iron-vacancy-ordered structure implies, in the absence of additional iron defects, that 1/5 of all iron ions are missing in comparison to the 122 system. The experimentally observed C4 rotational symmetry of I4/m further limits the possibility of alkali-metal vacancies to either none (all sites occupied) or one alkali-metal ion missing (1/5 of all alkali-metal ions) at the center of the simple tetragonal 122 unit cell, shown in Fig. 2.1a. These two considerations imply that the only possible chemical compositions of the antiferromagnetic phase are $A_xFe_{1.6}Se_2$, with x equal to either 1 or 0.8. Recent STM/STS measurements on thin films of $K_2Fe_4Se_5$ have confirmed the absence of Fe and Se defects in the antiferromagnetic phase [124]. This study also found a slightly different intensity at every fifth potassium site, which would suggest the $x = 0.8$ composition but this evidence remained inconclusive due to possible masking electronic effects. The $x = 0.8$ composition also seems to be consistent with the ratio of ^{37}Rb NMR intensities in the superconducting and antiferromagnetic phase [113].

Early neutron diffraction measurements established that the 122 iron chalcogenides undergo almost simultaneous structural and magnetic-ordering transitions at a very high temperature on the order of 550 K [133]. It was also discovered that these compounds possess a magnetic moment on iron atoms of about $3.3 \mu_B$ [133], which is unusually large for the iron pnictides. Moreover, this ordered antiferromagnetic moment was found to be aligned along the crystallographic c -axis, in contrast to its in-plane orientation in all other magnetically ordered iron-based materials [8], and susceptible to superconductivity, which indicates a certain degree of interplay between these two phases [133]. In the same neutron diffraction study an unusual antiferromagnetic ground state was revealed, which featured clustering of iron ions into plaquettes of four, ordered ferromagnetically within the plaquettes and antiferromagnetically between them, as shown in Fig. 2.11a. This exotic ground state was quickly confirmed by the first-principles calculations of the electronic and magnetic structure of the 245 materials [131]. These *ab initio* calculations also predicted that the antiferromagnetically ordered phase is a semiconductor with a direct band gap of ≈ 0.5 eV. In subsequent measurements of the optical conductivity of $Rb_2Fe_4Se_5$ a direct band gap was indeed identified [119], with a value of 0.45 eV, very close to the predicted value. The semiconducting and metallic optical properties of $Rb_2Fe_4Se_5$ will be considered in more detail in Sect. 4.3.

The properties of the minority metallic phase, unlike those of the antiferromagnetic phase, have seen much debate. Even the chemical composition of the metallic phase long remained a mystery. Opinions ranged from the stoichiometric 122 composition identical to that of the 122 iron arsenides (see e.g. Ref. [124]) to the chemical composition of the antiferromagnetic phase but without iron-vacancy order [134]. It is worth noting that while the latter implies rather moderate doping levels (depending on the relative concentrations of the alkaline metal and Fe with respect to the fully compensated 245 composition), the former case would result in a doping level of 0.5 electron per Fe lattice site (including the iron-vacancy sites), which corresponds to an extremely overdoped case of the 122 iron arsenides, beyond the superconducting dome in Fig. 2.4 for $Ba(Fe_{1-x}Co_x)_2As_2$. This debate has now largely been settled by

a combination of an ARPES study [67], theoretical RPA calculations [135], INS [84, 85], and NMR measurements [113], which have provided compelling evidence for the $A_{0.3}\text{Fe}_2\text{Se}_2$ composition of the superconducting phase. It corresponds to a doping level of 0.15 electrons per Fe atom, much closer to the optimal doping level of $\text{Ba}(\text{Fe}_{1-x}\text{Co}_x)_2\text{As}_2$ (a doping level of 0.15 electrons per Fe atom corresponds to $x = 0.3$ on the phase diagram of $\text{Ba}(\text{Fe}_{1-x}\text{Co}_x)_2\text{As}_2$ in Fig. 2.4). The same $A_{0.3}\text{Fe}_2\text{Se}_2$ composition of the metallic phase seems to stabilize in the $A_x\text{Fe}_{2-y}\text{Se}_2$ iron chalcogenides regardless of the type of the intercalating alkaline metal ($A = \text{K}$, Rb , and Cs) [85]. We would also like to point out that while the first ARPES measurements on a $\text{K}_2\text{Fe}_4\text{Se}_5$ superconductor, mentioned above, discovered the absence of hole pockets at the center of the Brillouin zone (and, in fact, the absence of any holelike Fermi-surface sheets whatsoever) at $k_z = 0$, as shown in Fig. 2.7I, subsequent measurements at $k_z = \pi$ revealed an additional electronlike pocket at the Z point of the Brillouin zone, illustrated schematically in Fig. 2.11b. The latter study also discovered nodeless superconducting gaps on all Fermi surfaces, with the central pocket developing a gap of 5 meV and the corner pockets a gap of 10 meV (see Fig. 2.11c). Recent STM/STS measurements on thin films of the same material have found twice smaller gaps [124].

Phase separation in the 122 iron chalcogenides makes the extensive investigation of this system with the entire arsenal of experimental condensed-matter research challenging, most prominently due to the intrinsic volume-averaging character of many experimental techniques, such as optics. In the latter case, useful information about the properties of the superconducting phase can only be extracted by resorting to an effective-medium approximation [121, 122], which, however, requires the detailed knowledge of the geometry and volume fraction of the minority phase. Fortunately,

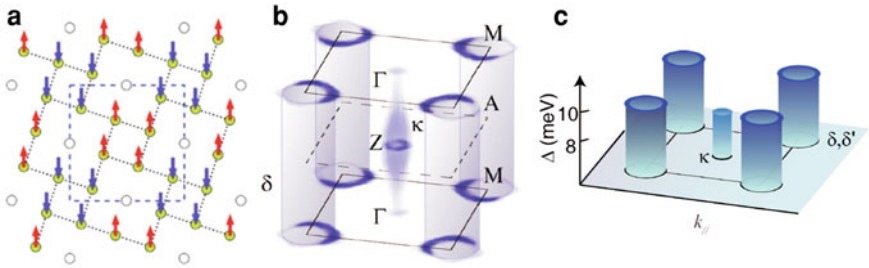


Fig. 2.11 **a** Block-checkerboard-type antiferromagnetic ground state of the $A_x\text{Fe}_{2-y}\text{Se}_2$ compounds identified in first-principles magnetic calculations based on experimentally obtained crystallographic structure. This magnetic pattern comprises clusters of four ferromagnetically coupled iron magnetic moments, with the clusters coupled antiferromagnetically between themselves. **b** Schematic representation of the complete Fermi surface of the 122 iron-chalcogenide superconductors obtained with ARPES. Note the absence of any Fermi pockets at the Γ point of the 2-Fe Brillouin zone and a small electronlike Fermi surface sheet at the Z point. **c** Superconducting gaps observed with ARPES at $k_z = \pi$ on the Fermi surfaces denoted as δ and κ in **b**. Panels **a**, **b**, and **c** are figures reprinted with permission from Refs. [131], [116], and [132], respectively. Copyright (2011, 2012) by the American Physical Society

many imaging and scanning techniques (STM/STS, ARPES, s-SNOM) possess a sufficient spatial resolution to be able to probe the superconducting and antiferromagnetic phases separately, thus providing reliable information about their properties. First ARPES measurements carried out on a $\text{K}_2\text{Fe}_4\text{Se}_5$ compound revealed sizable electron pockets of the Fermi surface at the corners of the 2-Fe Brillouin zone but observed no holelike pockets at its Γ point, as shown in Fig. 2.71, thus excluding the likely realized in most other iron-based superconductors extended s-wave (s_{\pm}) symmetry of the superconducting order parameter originating from spin-fluctuation-induced pairing enhanced by the nesting of holelike pockets at the center and electronlike pockets at the corners of the Brillouin zone. In the absence of holelike Fermi pockets at the center of the Brillouin zone one can still achieve spin-fluctuation-mediated superconductivity under the assumption of a $d_{x^2-y^2}$ superconducting order parameter in the unfolded 1-Fe Brillouin zone [135–137]. Since there are no Fermi pockets along the nodal lines of this type of the order parameter, the resulting superconducting state would be fully gapped (without nodes) in the unfolded Brillouin zone. However, one should bear in mind that the unfolded Brillouin zone, while quite useful in the analysis of magnetic properties, is a convenient abstraction and in reality the body-centered tetragonal symmetry of the iron-based superconductors leads to its folding along the $\mathbf{Q} = (\pi, \pi, \pi)$ vector of the reciprocal space, as can be inferred from Fig. 2.3. Given a fully gapped d -wave state in the unfolded Brillouin zone, the aforementioned folding would lead to an overlap and hybridization of the Fermi surfaces with the ‘+’ and ‘−’ sign of superconducting order parameter, which would obviously result in the formation of nodes [136], as shown in Fig. 2.12. As a consequence, the same (hybridized) Fermi surface would exhibit both positive and negative values of the superconducting gap. These considerations appear to be supported by recent INS measurements combined with calculations in the random-phase approximation [84], which explained the unusual quadruple structure of the neutron resonance peak in the superconducting state shown in Fig. 2.12 in the itinerant picture as a result of enhanced quasiparticle interaction between the well-nested portions of the Fermi pockets with the opposite signs of the superconducting gap (Fig. 2.12). However, this picture has been challenged by a recent ARPES study carried out at the out-of-plane wave vector $k_z = \pi$ [132], already mentioned above, which revealed nodeless superconducting gaps on all electron Fermi surfaces, including the small electron pocket at the Z point of the 2-Fe Brillouin zone (Figs. 2.11b, c). If the symmetry of the superconducting order parameter were indeed d -wave in the unfolded Brillouin zone (with its hybridized counterpart in the folded Brillouin zone), this small electron pocket would necessarily exhibit nodes by symmetry (see Fig. 2.12a).

As a matter of conclusion, we would like to comment on the issue of whether the separation of the superconducting and antiferromagnetic phases is extrinsic (thus allowing for the superconducting phase to be isolated) or intrinsic (implying that the superconducting phase only exists in the proximity of the antiferromagnetic phase and not by itself). Although the practice of experimental condensed-matter research shows that macroscopic phase separation is often an indication of the low quality of single crystals in view, in the case of the 122 iron chalcogenides, significant experimental evidence points towards the inherent character of the coexistence of

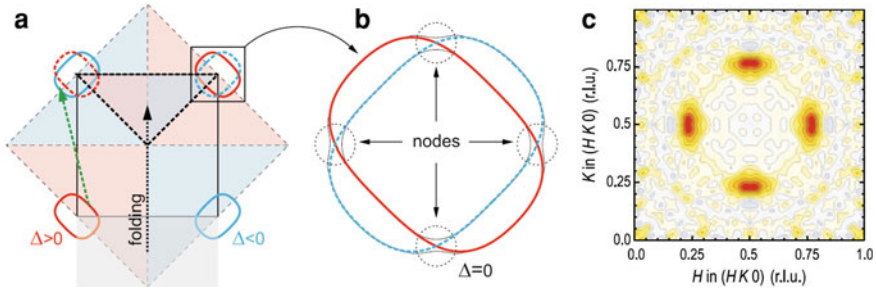


Fig. 12.12 **a** Fermi surface and the schematic structure of the superconducting order parameter in the $A_x\text{Fe}_{2-y}\text{Se}_2$ superconductors. The spin-fluctuation-mediated interaction leads to a $d_{x^2-y^2}$ -wave symmetry of the superconducting gap in the unfolded Brillouin zone (dashed square) [135, 136], illustrated here as a positive (red Fermi surface) and negative (blue Fermi surface) superconducting gap in the respective quadrants of the Brillouin zone. Since the $(\pm\pi, \pm\pi)$ nodal lines (dashed lines) connecting the corners of the unfolded Brillouin zone do not cross any of the Fermi surfaces, the superconducting gap exhibits no nodes. However, when the full body-centered tetragonal symmetry is taken into account, the hypothetical unfolded Brillouin zone is folded along the $\mathbf{Q} = (\pi, \pi, \pi)$ vector, whose in-plane projection is shown here as a black dotted arrow. The smaller, folded Brillouin zone (black square) is formed by making equivalent all parts of the unfolded Brillouin zone connected by the folding vector, i.e. the gray shaded area is transferred by \mathbf{Q} to become the portion of the folded Brillouin zone marked with thick dashed lines. This process results in now two electronlike Fermi surfaces at the corners of the new Brillouin zone but obviously with different signs of the superconducting order parameter. **b** Result of the hybridization of the two electronlike pockets at each corner of the folded Brillouin zone. In the hybridization areas the superconducting gap must change its sign while remaining on the same Fermi surface and therefore must go through zero. **c** Neutron resonance mode detected in the superconducting state of $\text{Rb}_2\text{Fe}_4\text{Se}_5$. Reprinted figure with permission from Ref. [84]. Copyright (2012) by the American Physical Society. Similar features have been observed in other compounds of the $A_x\text{Fe}_{2-y}\text{Se}_2$ family ($A = \text{K}, \text{Rb}, \text{and Cs}$) in Refs. [22, 85, 86]. The unusual positions of the resonance peaks in the unfolded Brillouin zone can be shown to result from enhanced quasiparticle interaction between the well-nested portions of the Fermi surface (green dashed arrow in **a**) [84]

these two phases. Mössbauer measurements under pressure, carried out on single crystals of $\text{Rb}_2\text{Fe}_4\text{Se}_5$, have revealed that superconductivity and antiferromagnetism disappear *simultaneously* with increasing hydrostatic pressure [27]. Such a correlation would be quite unusual for two independent, macroscopically separated phases. In addition, this study observed only a negative pressure effect on the transition temperature, i.e. the latter only decreases with increasing pressure, which indicates that superconductivity in these chalcogenide materials is already ‘optimized’ to the top of the superconducting dome. A recent neutron diffraction study of a closely related $\text{TiFe}_{1.6}\text{Se}_2$ material showed that the majority phase acquires a completely different ground state in the presence of phase separation with a minority phase with disordered iron ions [138]. Such a pronounced coupling between these phases appears natural in view of their nanoscale separation in the out-of-plane direction [114], allowing them to interact via lattice strain. The authors of Ref. [138] further infer from their scanning transmission electron microscopy measurements that the c -axis

lattice parameter of the minority disordered phase is 2 % larger than that of the ordered phase, while the corresponding difference in the in-plane counterpart is less than 0.3 %. Bearing in mind the strong effect of the pnictogen/chalcogen height on the superconducting transition temperature, it appears possible that the role of the presence of the encapsulating antiferromagnetic phase in the superconductivity of the 122 iron chalcogenides is to optimize the crystallographic structure (chalcogen height) by creating effective internal pressure (changing the c -axis lattice parameter) and thus to maximize the superconducting transition temperature. This picture is supported by recent first-principles calculations [139], which revealed a strong influence of the Wyckoff lattice position of the alkaline-metal ion on the electronic properties of the 122 iron chalcogenides and suggested a compelling explanation for re-entrant superconductivity with an even higher superconducting transition temperature upon application of external pressure observed in these compounds [27]. If the role of internal pressure generated on the superconducting phase by the coexisting antiferromagnetic phase is indeed at the root of superconductivity in these materials, it would be impossible to isolate the superconducting phase in free space without applying external pressure. In fact, it means that perhaps the true chemical equivalent of the superconducting phase found in the $A_x\text{Fe}_{2-y}\text{Se}_2$ compounds has already been synthesized but remained completely overlooked because it showed no superconductivity due to the absence of the aforementioned pressure-induced optimization of the c -axis lattice parameter.

References

1. Kamihara, Y., et al. (2006). Iron-based layered superconductor: LaOFeP . *Journal of the American Chemical Society*, 128, 10012–10013.
2. Kamihara, Y., Watanabe, T., Hirano, M., & Hosono, H. (2008). Iron-based layered superconductor $\text{La}[\text{O}_{1-x}\text{F}_x]\text{FeAs}$ ($x = 0.05 - 0.12$) with $T_c = 26$ K. *Journal of the American Chemical Society*, 130, 3296.
3. Nagamatsu, J., Nakagawa, N., Muranaka, T., Zenitani, Y., & Akimitsu, J. (2001). Superconductivity at 39 K in magnesium diboride. *Nature*, 410, 63–64.
4. Zhi-An, R., et al. (2008). Superconductivity at 55 K in iron-based F-doped layered quaternary compound $\text{Sm}[\text{O}_{1-x}\text{F}_x]\text{FeAs}$. *Chinese Physics Letters*, 25, 2215.
5. Rotter, M., Tegel, M., & Johrendt, D. (2008). Superconductivity at 38 K in the iron arsenide $(\text{Ba}_{1-x}\text{K}_x)\text{Fe}_2\text{As}_2$. *Physical Review Letters*, 101, 107006.
6. Chu, C. W. (2009). High-temperature superconductivity: alive and kicking. *Nature Physics*, 5, 787–789.
7. Bacsá, J., et al. (2011). Cation vacancy order in the $\text{K}_{0.8+x}\text{Fe}_{1.6-y}\text{Se}_2$ system: five-fold cell expansion accommodates 20 % tetrahedral vacancies. *Chemical Science*, 2, 1054.
8. Johnston, D. C. (2010). The puzzle of high temperature superconductivity in layered iron pnictides and chalcogenides. *Advances in Physics*, 59, 803.
9. Inosov, D. S., et al. (2011). Crossover from weak to strong pairing in unconventional superconductors. *Physical Review B*, 83, 214520.
10. Rotter, M., et al. (2008). Spin-density-wave anomaly at 140 K in the ternary iron arsenide BaFe_2As_2 . *Physical Review B*, 78, 020503.
11. Song, C.-L., et al. (2012). Suppression of superconductivity by twin boundaries in FeSe . *Physical Review Letters*, 109, 137004.

12. Kimber, S. A. J., et al. (2009). Similarities between structural distortions under pressure and chemical doping in superconducting BaFe_2As_2 . *Nature Materials*, 8, 471–475.
13. Guo, Y., et al. (2012). Continuous critical temperature enhancement with gradual hydrogen doping in $\text{LaFeAsO}_{0.85}\text{H}_x$ ($x = 0 - 0.85$). *Physical Review B*, 86, 054523.
14. Kittel, C. (2004). *Introduction to solid state physics*. New York: Wiley.
15. Park, J. T., et al. (2010). Symmetry of spin excitation spectra in the tetragonal paramagnetic and superconducting phases of 122-ferropnictides. *Physical Review B*, 82, 134503.
16. Marcinkova, A., et al. (2010). Superconductivity in $\text{NdFe}_{1-x}\text{Co}_x\text{AsO}$ ($0.05 \leq x \leq 0.20$) and rare-earth magnetic ordering in NdCoAsO . *Physical Review B*, 81, 064511.
17. McGuire, M. A., Sefat, A. S., Sales, B. C., & Mandrus, D. (2010). Iron substitution in NdCoAsO : crystal structure and magnetic phase diagram. *Physical Review B*, 82, 092404.
18. Li, Y. K., et al. (2012). Magnetic phase diagram in the Co-rich side of the $\text{LCo}_{1-x}\text{Fe}_x\text{AsO}$ ($\text{L} = \text{La}, \text{Sm}$) system. *Physical Review B*, 86, 104408.
19. Christianson, A. D., et al. (2008). Unconventional superconductivity in $\text{Ba}_{0.6}\text{K}_{0.4}\text{Fe}_2\text{As}_2$ from inelastic neutron scattering. *Nature*, 456, 930.
20. Inosov, D. S., et al. (2009). Normal-state spin dynamics and temperature-dependent spin-resonance energy in optimally doped $\text{BaFe}_{1.85}\text{Co}_{0.15}\text{As}_2$. *Nature Physics*, 6, 178.
21. Popovich, P., et al. (2010). Specific heat measurements of $\text{Ba}_{0.68}\text{K}_{0.32}\text{Fe}_2\text{As}_2$ single crystals: evidence for a multiband strong-coupling superconducting state. *Physical Review Letters*, 105, 027003.
22. Park, J. T., et al. (2011). Magnetic resonant mode in the low-energy spin-excitation spectrum of superconducting $\text{Rb}_2\text{Fe}_4\text{Se}_5$ single crystals. *Physical Review Letters*, 107, 177005.
23. Charnukha, A., et al. (2011). Eliashberg approach to infrared anomalies induced by the superconducting state of $\text{Ba}_{0.68}\text{K}_{0.32}\text{Fe}_2\text{As}_2$ single crystals. *Physical Review B*, 84, 174511.
24. Lee, G., et al. (2012). Orbital selective Fermi surface shifts and mechanism of high T_c superconductivity in correlated AFeAs ($\text{A} = \text{Li}, \text{Na}$). *Physical Review Letters*, 109, 177001.
25. Gati, E., et al. (2012). Hydrostatic-pressure tuning of magnetic, nonmagnetic, and superconducting states in annealed $\text{Ca}(\text{Fe}_{1-x}\text{Co}_x)_2\text{As}_2$. *Physical Review B*, 86, 220511.
26. Stewart, G. R. (2011). Superconductivity in iron compounds. *Reviews of Modern Physics*, 83, 1589–1652.
27. Ksenofontov, V., et al. (2012). Superconductivity and magnetism in $\text{Rb}_{0.8}\text{Fe}_{1.6}\text{Se}_2$ under pressure. *Physical Review B*, 85, 214519.
28. Marsik, P., et al. (2010). Coexistence and competition of magnetism and superconductivity on the nanometer scale in underdoped $\text{BaFe}_{1.89}\text{Co}_{0.11}\text{As}_2$. *Physical Review Letters*, 105, 057001.
29. Park, J. T., et al. (2009). Electronic phase separation in the slightly underdoped iron pnictide superconductor $(\text{Ba}_{1-x}\text{K}_x)\text{Fe}_2\text{As}_2$. *Physical Review Letters*, 102, 117006.
30. Li, Z., et al. (2012). Microscopic coexistence of antiferromagnetic order and superconductivity in $\text{Ba}_{0.77}\text{K}_{0.23}\text{Fe}_2\text{As}_2$. *Physical Review B*, 86, 180501.
31. Avci, S., et al. (2012). Phase diagram of $\text{Ba}_{1-x}\text{K}_x\text{Fe}_2\text{As}_2$. *Physical Review B*, 85, 184507.
32. Ma, L., et al. (2012). Microscopic coexistence of superconductivity and antiferromagnetism in underdoped $\text{Ba}(\text{Fe}_{1-x}\text{Ru}_x)_2\text{As}_2$. *Physical Review Letters*, 109, 197002.
33. Hashimoto, K., et al. (2012). A sharp peak of the zero-temperature penetration depth at optimal composition in $\text{BaFe}_2(\text{As}_{1-x}\text{P}_x)_2$. *Science*, 336, 1554–1557.
34. Rotter, M., Pangerl, M., Tegel, M., & Johrendt, D. (2008). Superconductivity and crystal structures of $(\text{Ba}_{1-x}\text{K}_x)\text{Fe}_2\text{As}_2$ ($x = 0 - 1$). *Angewandte Chemie International Edition*, 47, 7949–7952.
35. Chu, J.-H., Analytis, J. G., Kucharczyk, C., & Fisher, I. R. (2009). Determination of the phase diagram of the electron-doped superconductor $\text{Ba}(\text{Fe}_{1-x}\text{Co}_x)_2\text{As}_2$. *Physical Review B*, 79, 014506.
36. Tinkham, M. (1995). *Introduction to superconductivity*. New York: McGraw-Hill.
37. Goldman, A. I., et al. (2008). Lattice and magnetic instabilities in CaFe_2As_2 : a single-crystal neutron diffraction study. *Physical Review B*, 78, 100506.
38. Ni, N., et al. (2008). First-order structural phase transition in CaFe_2As_2 . *Physical Review B*, 78, 014523.

39. Yan, J.-Q., et al. (2008). Structural transition and anisotropic properties of single-crystalline SrFe_2As_2 . *Physical Review B*, 78, 024516.
40. Loudon, J. C., Howell, C. J., Gillett, J., Sebastian, S. E., & Midgley, P. A. (2010). Determination of the nature of the tetragonal to orthorhombic phase transition in SrFe_2As_2 by measurement of the local order parameter. *Physical Review B*, 81, 214111.
41. Blomberg, E. C., et al. (2011). In-plane anisotropy of electrical resistivity in strain-detwinned SrFe_2As_2 . *Physical Review B*, 83, 134505.
42. Chu, J.-H., et al. (2010). In-plane resistivity anisotropy in an underdoped iron arsenide superconductor. *Science*, 329, 824–826.
43. Tanatar, M. A., et al. (2010). Uniaxial-strain mechanical detwinning of CaFe_2As_2 and BaFe_2As_2 crystals: optical and transport study. *Physical Review B*, 81, 184508.
44. Chu, J.-H., Kuo, H.-H., Analytis, J. G., & Fisher, I. R. (2012). Divergent nematic susceptibility in an iron arsenide superconductor. *Science*, 337, 710–712.
45. Kasahara, S., et al. (2012). Electronic nematicity above the structural and superconducting transition in $\text{BaFe}_2(\text{As}_{1-x}\text{P}_x)_2$. *Nature*, 486, 382–385.
46. Fernandes, R. M., Abrahams, E., & Schmalian, J. (2011). Anisotropic in-plane resistivity in the nematic phase of the iron pnictides. *Physical Review Letters*, 107, 217002.
47. Fernandes, R. M., Chubukov, A. V., Knolle, J., Eremin, I., & Schmalian, J. (2012). Preemptive nematic order, pseudogap, and orbital order in the iron pnictides. *Physical Review B*, 85, 024534.
48. Yi, M., et al. (2011). Symmetry-breaking orbital anisotropy observed for detwinned $\text{Ba}(\text{Fe}_{1-x}\text{Co}_x)_2\text{As}_2$ above the spin density wave transition. *Proceedings of the National Academy of Sciences*, 108, 6878–6883.
49. Damascelli, A., Hussain, Z., & Shen, Z.-X. (2003). Angle-resolved photoemission studies of the cuprate superconductors. *Reviews of Modern Physics*, 75, 473–541.
50. Sebastian, S. E. (2012). Quantum oscillations in iron pnictide superconductors. In N.L. Wang, H. Hosono, P. C. Dai (Eds.), *Iron-based superconductors—materials, properties and mechanisms*. Singapore: Pan Stanford Publishing.
51. Imada, M., Fujimori, A., & Tokura, Y. (1998). Metal-insulator transitions. *Reviews of Modern Physics*, 70, 1039–1263.
52. Charnukha, A., et al. (2011). Superconductivity-induced optical anomaly in an iron arsenide. *Nature Communications*, 2, 219.
53. Mazin, I. I., & Schmalian, J. (2009). Pairing symmetry and pairing state in ferropnictides: theoretical overview. *Physica C*, 469, 614–627.
54. Zabolotnyy, V. B., et al. (2009). (π, π) electronic order in iron arsenide superconductors. *Nature*, 457, 569–572.
55. Arnold, B. J., et al. (2011). Nesting of electron and hole Fermi surfaces in nonsuperconducting BaFe_2P_2 . *Physical Review B*, 83, 220504.
56. Basov, D. N., & Chubukov, A. V. (2011). Manifesto for a higher T_c . *Nature Physics*, 7, 272–276.
57. Evtushinsky, D. V., et al. (2009). Momentum dependence of the superconducting gap in $\text{Ba}_{1-x}\text{K}_x\text{Fe}_2\text{As}_2$. *Physical Review B*, 79, 054517.
58. Evtushinsky, D.V., et al. (2012). Strong pairing at iron $3d_{xz,yz}$ orbitals in hole-doped BaFe_2As_2 . arXiv:1204.2432 (unpublished).
59. Analytis, J. G., et al. (2009). Fermi surface of SrFe_2P_2 determined by the de Haas-van Alphen effect. *Physical Review Letters*, 103, 076401.
60. Carrington, A. (2011). Quantum oscillation studies of the Fermi surface of iron-pnictide superconductors. *Reports on Progress in Physics*, 74, 124507.
61. Analytis, J. G., Chu, J.-H., McDonald, R. D., Riggs, S. C., & Fisher, I. R. (2010). Enhanced Fermi-surface nesting in superconducting $\text{BaFe}_2(\text{As}_{1-x}\text{P}_x)_2$ revealed by de Haas-van Alphen effect. *Physical Review Letters*, 105, 207004.
62. Shishido, H., et al. (2010). Evolution of the Fermi surface of $\text{BaFe}_2(\text{As}_{1-x}\text{P}_x)_2$ on entering the superconducting dome. *Physical Review Letters*, 104, 057008.

63. Shan, L., et al. (2012). Evidence of a spin resonance mode in the iron-based superconductor $\text{Ba}_{0.6}\text{K}_{0.4}\text{Fe}_2\text{As}_2$ from scanning tunneling spectroscopy. *Physical Review Letters*, 108, 227002.
64. Dai, P., Hu, J., & Dagotto, E. (2012). Magnetism and its microscopic origin in iron-based high-temperature superconductors. *Nature Physics*, 8, 709–718.
65. Yoshida, T., et al. (2006). Systematic doping evolution of the underlying Fermi surface of $\text{La}_{2-x}\text{Sr}_x\text{CuO}_4$. *Physical Review B*, 74, 224510.
66. Xia, Y., et al. (2009). Fermi surface topology and low-lying quasiparticle dynamics of parent $\text{Fe}_{1+x}\text{Te/Se}$ superconductor. *Physical Review Letters*, 103, 037002.
67. Qian, T., et al. (2011). Absence of a holelike Fermi surface for the iron-based $\text{K}_{0.8}\text{Fe}_{1.7}\text{Se}_2$ superconductor revealed by angle-resolved photoemission spectroscopy. *Physical Review Letters*, 106, 187001.
68. Vagnin, D., et al. (1987). Antiferromagnetism in $\text{La}_2\text{CuO}_{4-y}$. *Physical Review Letters*, 58, 2802–2805.
69. Gruner, G. (2000). *Density waves in solids*. Westview Press, Boulder.
70. Fawcett, E. (1988). Spin-density-wave antiferromagnetism in chromium. *Reviews of Modern Physics*, 60, 209–283.
71. Schafgans, A. A., et al. (2012). Electronic correlations and unconventional spectral weight transfer in the high-temperature pnictide $\text{BaFe}_{2-x}\text{Co}_x\text{As}_2$ superconductor using infrared spectroscopy. *Physical Review Letters*, 108, 147002.
72. Harriger, L. W., et al. (2011). Nematic spin fluid in the tetragonal phase of BaFe_2As_2 . *Physical Review B*, 84, 054544.
73. Kaneshita, E., & Tohyama, T. (2010). Spin and charge dynamics ruled by antiferromagnetic order in iron pnictide superconductors. *Physical Review B*, 82, 094441.
74. Coldea, R., et al. (2001). Spin waves and electronic interactions in La_2CuO_4 . *Physical Review Letters*, 86, 5377–5380.
75. Grestarsson, H., et al. (2011). Revealing the dual nature of magnetism in iron pnictides and iron chalcogenides using X-ray emission spectroscopy. *Physical Review B*, 84, 100509.
76. Borisenko, S. V., et al. (2010). Superconductivity without nesting in LiFeAs . *Physical Review Letters*, 105, 067002.
77. Ishikawa, Y., Noda, Y., Uemura, Y. J., Majkrzak, C. F., & Shirane, G. (1985). Paramagnetic spin fluctuations in the weak itinerant-electron ferromagnet MnSi . *Physical Review B*, 31, 5884–5893.
78. Boeri, L., Dolgov, O. V., & Golubov, A. A. (2008). Is $\text{LaFeAsO}_{1-x}\text{F}_x$ an electron-phonon superconductor? *Physical Review Letters*, 101, 026403.
79. Moriya, T., & Ueda, K. (2003). Antiferromagnetic spin fluctuation and superconductivity. *Reports on Progress in Physics*, 66, 1299.
80. Scalapino, D. J., Loh, E., & Hirsch, J. E. (1986). *d*-wave pairing near a spin-density-wave instability. *Physical Review B*, 34, 8190–8192.
81. Tsuei, C. C., & Kirtley, J. R. (2000). Pairing symmetry in cuprate superconductors. *Reviews of Modern Physics*, 72, 969–1016.
82. Bennemann, K.-H., & Ketterson, J. B. (2008). *Superconductivity: volume 1: conventional and unconventional superconductors*. Springer, Berlin.
83. Zhang, C., et al. (2011). Neutron scattering studies of spin excitations in hole-doped $\text{Ba}_{0.67}\text{K}_{0.33}\text{Fe}_2\text{As}_2$ superconductor. *Science Reports*, 1, 115.
84. Friemel, G., et al. (2012). Reciprocal-space structure and dispersion of the magnetic resonant mode in the superconducting phase of $\text{Rb}_x\text{Fe}_{2-y}\text{Se}_2$ single crystals. *Physical Review B*, 85, 140511.
85. Friemel, G., et al. (2012). Conformity of spin fluctuations in alkali-metal iron selenide superconductors inferred from the observation of a magnetic resonant mode in $\text{K}_x\text{Fe}_{2-y}\text{Se}_2$. *Europhysics Letters*, 99, 67004.
86. Taylor, A. E., et al. (2012). Spin-wave excitations and superconducting resonant mode in $\text{Cs}_x\text{Fe}_{2-y}\text{Se}_2$. *Physical Review B*, 86, 094528.

87. Onari, S., Kontani, H., & Sato, M. (2010). Structure of neutron-scattering peaks in both s_{++} -wave and s_{\pm} -wave states of an iron pnictide superconductor. *Physical Review B*, *81*, 060504.
88. Annett, J. F. (1990). Symmetry of the order parameter for high-temperature superconductivity. *Advances in Physics*, *39*, 83–126.
89. Van Harlingen, D. J. (1995). Phase-sensitive tests of the symmetry of the pairing state in the high-temperature superconductors: evidence for $d_{x^2-y^2}$ symmetry. *Reviews of Modern Physics*, *67*, 515–535.
90. Hanaguri, T., Niitaka, S., Kuroki, K., & Takagi, H. (2010). Unconventional s -wave superconductivity in Fe(Se, Te). *Science*, *328*, 474.
91. Golubov, A. A., & Mazin, I. I. (2013). Designing phase-sensitive tests for Fe-based superconductors. *Applied Physics Letters*, *102*, 032601.
92. Shimojima, T., et al. (2010). Orbital-dependent modifications of electronic structure across the magnetostructural transition in BaFe_2As_2 . *Physical Review Letters*, *104*, 057002.
93. Sudayama, T., et al. (2011). Doping-dependent and orbital-dependent band renormalization in $\text{Ba}(\text{Fe}_{1-x}\text{Co}_x)_2\text{As}_2$ superconductors. *Journal of the Physical Society of Japan*, *80*, 113707.
94. Arham, H. Z., et al. (2012). Detection of orbital fluctuations above the structural transition temperature in the iron pnictides and chalcogenides. *Physical Review B*, *85*, 214515.
95. Kontani, H., & Onari, S. (2010). Orbital-fluctuation-mediated superconductivity in iron pnictides: analysis of the five-orbital Hubbard–Holstein model. *Physical Review Letters*, *104*, 157001.
96. Yamada, T., & Ōno, Y. (2012). Dynamical mean-field study of local pairing interaction mediated by spin and orbital fluctuations in iron pnictide superconductors. arXiv:1209.4954 (unpublished).
97. Hardy, F., et al. (2010). Doping evolution of superconducting gaps and electronic densities of states in $\text{Ba}(\text{Fe}_{1-x}\text{Co}_x)_2\text{As}_2$ iron pnictides. *Europhysics Letters*, *91*, 47008.
98. Grimvall, G. (1976). The electron-phonon interaction in normal metals. *Physica Scripta*, *14*, 63.
99. Grimvall, G. (1981). In: E.P. Wohlfarth (Ed.), *The electron–phonon interaction in metals, selected topics in solid state physics*, North-Holland, Amsterdam.
100. Suhl, H., Matthias, B. T., & Walker, L. R. (1959). Bardeen–Cooper–Schrieffer theory of superconductivity in the case of overlapping bands. *Physical Review Letters*, *3*, 552–554.
101. Dolgov, O. V., Mazin, I. I., Parker, D., & Golubov, A. A. (2009). Interband superconductivity: contrasts between Bardeen–Cooper–Schrieffer and Eliashberg theories. *Physical Review B*, *79*, 060502.
102. Nicol, E. J., Carbotte, J. P., & Timusk, T. (1991). Optical conductivity in high- T_c superconductors. *Physical Review B*, *43*, 473–479.
103. Guo, J., et al. (2010). Superconductivity in the iron selenide $\text{K}_x\text{Fe}_2\text{Se}_2$ ($0 \leq x \leq 1.0$). *Physical Review B*, *82*, 180520.
104. Ying, J. J., et al. (2011). Superconductivity and magnetic properties of single crystals of $\text{K}_{0.75}\text{Fe}_{1.66}\text{Se}_2$ and $\text{Cs}_{0.81}\text{Fe}_{1.61}\text{Se}_2$. *Physical Review B*, *83*, 212502.
105. Li, C.-H., Shen, B., Han, F., Zhu, X., & Wen, H.-H. (2011). Transport properties and anisotropy of $\text{Rb}_{1-x}\text{Fe}_{2-y}\text{Se}_2$ single crystals. *Physical Review B*, *83*, 184521.
106. Mizuguchi, Y., et al. (2011). Transport properties of the new Fe-based superconductor $\text{K}_x\text{Fe}_2\text{Se}_2$ ($T_c = 33\text{K}$). *Applied Physics Letters*, *98*, 042511.
107. Wang, A. F., et al. (2011). Superconductivity at 32 K in single-crystalline $\text{Rb}_x\text{Fe}_{2-y}\text{Se}_2$. *Physical Review B*, *83*, 060512.
108. Fang, M.-H., et al. (2011). Fe-based superconductivity with $T_c = 31\text{K}$ bordering an antiferromagnetic insulator in $(\text{Ti}, \text{K})\text{Fe}_x\text{Se}_2$. *Europhysics Letters*, *94*, 27009.
109. Zhang, A. M., et al. (2012). Effect of iron content and potassium substitution in $\text{A}_{0.8}\text{Fe}_{1.6}\text{Se}_2$ ($\text{A}=\text{K}, \text{Rb}, \text{Ti}$) superconductors: a Raman scattering investigation. *Physical Review B*, *86*, 134502.
110. Tsurkan, V., et al. (2011). Anisotropic magnetism, superconductivity, and the phase diagram of $\text{Rb}_{1-x}\text{Fe}_{2-y}\text{Se}_2$. *Physical Review B*, *84*, 144520.

111. Ksenofontov, V., et al. (2011). Phase separation in superconducting and antiferromagnetic $\text{Rb}_{0.8}\text{Fe}_{1.6}\text{Se}_2$ probed by Mössbauer spectroscopy. *Physical Review B*, 84, 180508.
112. Shermadini, Z., et al. (2012). Superconducting properties of single-crystalline $\text{A}_x\text{Fe}_{2-y}\text{Se}_2$ ($\text{A} = \text{Rb}, \text{K}$) studied using muon spin spectroscopy. *Physical Review B*, 85, 100501.
113. Texier, Y., et al. (2012). NMR study in the iron-selenide $\text{Rb}_{0.74}\text{Fe}_{1.6}\text{Se}_2$: determination of the superconducting phase as iron vacancy-free $\text{Rb}_{0.3}\text{Fe}_2\text{Se}_2$. *Physical Review Letters*, 108, 237002.
114. Charnukha, A., et al. (2012). Nanoscale layering of antiferromagnetic and superconducting phases in $\text{Rb}_2\text{Fe}_4\text{Se}_5$ single crystals. *Physical Review Letters*, 109, 017003.
115. Liu, Y., Xing, Q., Dennis, K. W., McCallum, R. W., & Lograsso, T. A. (2012). Evolution of precipitate morphology during heat treatment and its implications for the superconductivity in $\text{K}_x\text{Fe}_{1.6+y}\text{Se}_2$ single crystals. *Physical Review B*, 86, 144507.
116. Chen, F., et al. (2011). Electronic identification of the parental phases and mesoscopic phase separation of $\text{K}_x\text{Fe}_{2-y}\text{Se}_2$ superconductors. *Physical Review X*, 1, 021020.
117. Ricci, A., et al. (2011). Nanoscale phase separation in the iron chalcogenide superconductor $\text{K}_{0.8}\text{Fe}_{1.6}\text{Se}_2$ as seen via scanning nanofocused X-ray diffraction. *Physical Review B*, 84, 060511.
118. Cai, P., et al. (2012). Imaging the coexistence of a superconducting phase and a charge-density modulation in the $\text{K}_{0.73}\text{Fe}_{1.67}\text{Se}_2$ superconductor using a scanning tunneling microscope. *Physical Review B*, 85, 094512.
119. Charnukha, A., et al. (2012). Optical conductivity of superconducting $\text{Rb}_2\text{Fe}_4\text{Se}_5$ single crystals. *Physical Review B*, 85, 100504.
120. Homes, C. C., Xu, Z. J., Wen, J. S., & Gu, G. D. (2012). Optical conductivity of superconducting $\text{K}_{0.8}\text{Fe}_{2-y}\text{Se}_2$ single crystals: evidence for a Josephson-coupled phase. *Physical Review B*, 85, 180510.
121. Homes, C. C., Xu, Z. J., Wen, J. S., & Gu, G. D. (2012). Effective medium approximation and the complex optical properties of the inhomogeneous superconductor $\text{K}_{0.8}\text{Fe}_{2-y}\text{Se}_2$. *Physical Review B*, 86, 144530.
122. Wang, C. N., et al. (2012). Macroscopic phase segregation in superconducting $\text{K}_{0.73}\text{Fe}_{1.67}\text{Se}_2$ as seen by muon spin rotation and infrared spectroscopy. *Physical Review B*, 85, 214503.
123. Lazarević, N., et al. (2012). Vacancy-induced nanoscale phase separation in $\text{K}_x\text{Fe}_{2-y}\text{Se}_2$ single crystals evidenced by Raman scattering and powder X-ray diffraction. *Physical Review B*, 86, 054503.
124. Li, W., et al. (2012). Phase separation and magnetic order in K-doped iron selenide superconductor. *Nature Physics*, 8, 126–130.
125. Li, W., et al. (2012). KFe_2Se_2 is the parent compound of K-doped iron selenide superconductors. *Physical Review Letters*, 109, 057003.
126. Simonelli, L., et al. (2012). Coexistence of different electronic phases in the $\text{K}_{0.8}\text{Fe}_{1.6}\text{Se}_2$ superconductor: a bulk-sensitive hard X-ray spectroscopy study. *Physical Review Letters*, 85, 224510.
127. Weyeneth, S., et al. (2012). Superconductivity and magnetism in $\text{Rb}_x\text{Fe}_{2-y}\text{Se}_2$: impact of thermal treatment on mesoscopic phase separation. *Physical Review B*, 86, 134530.
128. Yuan, R. H., et al. (2012). Nanoscale phase separation of antiferromagnetic order and superconductivity in $\text{K}_{0.75}\text{Fe}_{1.75}\text{Se}_2$. *Science Reports*, 2, 221.
129. Shoemaker, D. P., et al. (2012). Phase relations in $\text{K}_x\text{Fe}_{2-y}\text{Se}_2$ and the structure of superconducting $\text{K}_x\text{Fe}_2\text{Se}_2$ via high-resolution synchrotron diffraction. *Physical Review B*, 86, 184511.
130. Wen, H.-H. (2012). Overview on the physics and materials of the new superconductor $\text{K}_x\text{Fe}_{2-y}\text{Se}_2$. *Reports on Progress in Physics*, 75, 112501.
131. Yan, X.-W., Gao, M., Lu, Z.-Y., & Xiang, T. (2011). Ternary iron selenide $\text{K}_{0.8}\text{Fe}_{1.6}\text{Se}_2$ is an antiferromagnetic semiconductor. *Physical Review B*, 83, 233205.
132. Xu, M., et al. (2012). Evidence for an s -wave superconducting gap in $\text{K}_x\text{Fe}_{2-y}\text{Se}_2$ from angle-resolved photoemission. *Physical Review B*, 85, 220504.

133. Bao, W., et al. (2011). A novel large moment antiferromagnetic order in $\text{K}_{0.8}\text{Fe}_{1.6}\text{Se}_2$ superconductor. *Chinese Physics Letters*, 28, 086104.
134. Wang, Z., et al. (2011). Microstructure and ordering of iron vacancies in the superconductor system $\text{K}_y\text{Fe}_x\text{Se}_2$ as seen via transmission electron microscopy. *Physical Review B*, 83, 140505.
135. Maier, T. A., Graser, S., Hirschfeld, P. J., & Scalapino, D. J. (2011). d -wave pairing from spin fluctuations in the $\text{K}_x\text{Fe}_{2-y}\text{Se}_2$ superconductors. *Physical Review B*, 83, 100515.
136. Saito, T., Onari, S., & Kontani, H. (2011). Emergence of fully gapped s_{++} -wave and nodal d -wave states mediated by orbital and spin fluctuations in a ten-orbital model of KFe_2Se_2 . *Physical Review B*, 83, 140512.
137. Wang, F., et al. (2011). The electron pairing of $\text{K}_x\text{Fe}_{2-y}\text{Se}_2$. *Europhysics Letters*, 93, 57003.
138. May, A. F., et al. (2012). Spin reorientation in $\text{TlFe}_{1.6}\text{Se}_2$ with complete vacancy ordering. *Physical Review Letters*, 109, 077003.
139. Yan, X.-W., & Gao, M. (2012). The effect of the Wyckoff position of the K atom on the crystal structure and electronic properties of the compound KFe_2Se_2 . *Journal of Physics: Condensed Matter*, 24, 455702.

Charge Dynamics in 122 Iron-Based Superconductors

Charnukha, A.

2014, XI, 130 p. 43 illus., 24 illus. in color., Hardcover

ISBN: 978-3-319-01191-2